

1 **Diagnosing the thickness-weighted averaged eddy-mean**
2 **flow interaction from an eddying North Atlantic**
3 **ensemble, Part I: The Eliassen–Palm flux**

4 **Takaya Uchida¹, Quentin Jamet¹, William K. Dewar^{1,2}, Julien Le Sommer¹,**
5 **Thierry Penduff¹ & Dhruv Balwada³**

6 ¹Université Grenoble Alpes, CNRS, IRD, Grenoble-INP, Institut des Géosciences de l'Environnement,
7 France

8 ²Department of Earth, Ocean and Atmospheric Science, Florida State University, USA

9 ³Lamont-Doherty Earth Observatory, Columbia University in the City of New York, USA

10 **Key Points:**

- 11 • Eddying ensemble runs of the North Atlantic Ocean are used to diagnose the thickness-
12 weighted averaged eddy-mean flow interaction.
- 13 • A dynamically-consistent approximately neutral surface is implemented to define
14 the buoyancy coordinate for a realistic equation of state.
- 15 • The Eliassen-Palm flux convergence implies a tendency to force a poleward mi-
16 gration of the Gulf Stream.

Corresponding author: Takaya Uchida, takaya.uchida@univ-grenoble-alpes.fr

17 **Abstract**

18 The thickness-weighted average (TWA) framework, which treats the residual-mean flow
 19 as the prognostic variable, provides a clear theoretical formulation of the eddy feedback
 20 onto the residual-mean flow. The averaging operator involved in the TWA framework,
 21 although in theory being an ensemble mean, in practice has often been approximated
 22 by a temporal mean. Here, we analyze an ensemble of North Atlantic simulations at mesoscale-
 23 permitting resolution ($1/12^\circ$). We therefore recognize means and eddies in terms of en-
 24 semble means and fluctuations about those means. The ensemble dimension being or-
 25 thogonal to the temporal and spatial dimensions negates the necessity for an arbitrary
 26 temporal or spatial scale in defining the eddies. Eddy-mean flow feedbacks are encap-
 27 sulated in the Eliassen-Palm (E-P) flux tensor and its convergence indicates that eddy
 28 momentum fluxes dominate in the separated Gulf Stream. The eddies can be interpreted
 29 to contribute to the zonal meandering of the Gulf Stream and a northward migration
 30 of it in the meridional direction. Downstream of the separated Gulf Stream in the North
 31 Atlantic Current region, the interfacial form stress convergence becomes leading order
 32 in the E-P flux convergence.

33 **Plain Language Summary**

34 We have greatly benefited from global climate simulations in gaining insight into
 35 what the climate would look like in an ever warming future. Due to computational con-
 36 straints, however, the oceanic component of such simulations have been poorly constrained.
 37 The storm systems of the ocean, often referred to as eddies, defined as fluctuations about
 38 jets such as the Gulf Stream and meandering of the jet itself, have remained challeng-
 39 ing to accurately simulate on a global scale. Although relatively small in scale compared
 40 to the global ocean, eddies have been known to modulate the climate by transporting
 41 heat from the equator to the poles. By running a regional simulation of the North At-
 42 lantic Ocean and taking advantage of recent theoretical developments, we implement a
 43 new framework to evaluate such simulations in representing the Gulf Stream.

44 **1 Introduction**

45 Eddy-mean flow interaction has been a key framework in understanding jet forma-
 46 tion in geophysical flows such as in the atmosphere and ocean (Bühler, 2014; Vallis, 2017).
 47 A prominent example of such a jet in the North Atlantic ocean is the Gulf Stream. Pre-
 48 vious studies have shown how eddies fluxing buoyancy and momentum back into the mean

49 flow energize the western boundary currents including the Gulf Stream (Lévy et al., 2010;
50 Waterman & Lilly, 2015; Chassignet & Xu, 2017; Aluie et al., 2018). Basin-scale sim-
51 ulations, however, often lack sufficient spatial resolution to accurately resolve the eddies
52 and hence, result in underestimating the eddy fluxes of momentum and tracers (Capet
53 et al., 2008b; Arbic et al., 2013; Kjellsson & Zanna, 2017; Balwada et al., 2018; Uchida
54 et al., 2019; Schubert et al., 2020). Due to computational constraints, we will continue
55 to rely on models which only partially resolve the mesoscale, a scale roughly on the or-
56 der of O(20-200 km) at which the ocean currents are most energetic (Stammer, 1997; Xu
57 & Fu, 2011, 2012; Ajayi et al., 2020), for global ocean and climate simulations. As a re-
58 sult, there has been an on-going effort to develop energy-backscattering eddy parametriza-
59 tions which incorporate the dynamical effects of eddy momentum fluxes due to other-
60 wise unresolved mesoscale turbulence (e.g. Kitsios et al., 2013; Zanna et al., 2017; Berloff,
61 2018; Bachman et al., 2018; Bachman, 2019; Jansen et al., 2019; Perezhogin, 2019; Zanna
62 & Bolton, 2020; Juricke et al., 2020; Guillaumin & Zanna, 2021; Uchida et al., 2022).

63 There has been less emphasis, however, on quantifying the spatial and temporal
64 characteristics of the eddy buoyancy and momentum fluxes themselves, which the parametriza-
65 tions are deemed to represent. The focus of this study is, therefore, to examine the dy-
66 namical effects of mesoscale turbulence on the mean flow in realistic, partially air-sea cou-
67 pled, eddy ensemble runs of the North Atlantic. The thickness-weighted average (TWA)
68 framework, which treats the residual-mean velocity as a prognostic variable, allows for
69 a straightforward theoretical expression of the eddy feedback onto the residual-mean flow
70 (e.g. Gallimore & Johnson, 1981; Andrews, 1983; de Szoeke & Bennett, 1993; McDougall
71 & McIntosh, 2001; Young, 2012; Maddison & Marshall, 2013; Aoki, 2014). It is well known
72 in the atmospheric and Southern Ocean literature that it is the residual-mean flow, which
73 is the residual that emerges upon the partial cancellation between the Eulerian mean flow
74 and eddies, that captures the ‘mean’ flow for heat and tracer transport (Bühler, 2014;
75 Vallis, 2017). The TWA framework has been fruitful in examining eddy-mean flow in-
76 teraction in idealized modelling studies (e.g. D. P. Marshall et al., 2012; Cessi & Wolfe,
77 2013; Ringler et al., 2017; Bire & Wolfe, 2018). Here, we extend these studies to a re-
78 alistic simulation of the North Atlantic. We will examine the TWA eddy diffusivities and
79 mode water formation in subsequent papers.

80 To our knowledge, Aiki and Richards (2008), Aoki et al. (2016), Stanley (2018) and
81 Zhao and Marshall (2020) are the only studies that diagnose the TWA framework in re-

82 alistic ocean simulations. Aiki and Richards (2008), however, recompute the hydrostatic
 83 pressure using potential density for their off-line diagnosis in defining their buoyancy co-
 84 ordinate, which can result in significant discrepancies from the pressure field used in their
 85 on-line calculation and consequently errors in the diagnosed geostrophic shear. Although
 86 Aoki et al. (2016) negate this complication between the buoyancy coordinate and mean
 87 pressure field by analyzing their outputs in geopotential coordinates, they compute the
 88 eddy component of the pressure term (F^+ in their paper) using potential density, result-
 89 ing in errors in the interfacial form stress (viz. this violates equation (10) described be-
 90 low for ϕ' and m'). Their truncation in Taylor expansion about the mean position of buoy-
 91 ancy surfaces for the sake of convenience in diagnosing the residual-mean flow in geopo-
 92 tential coordinates limits the accuracy of the eddy terms. Lastly, all four studies assume
 93 ergodicity. The ergodic assumption of treating a temporal mean equivalent to an ensem-
 94 ble mean, although a pragmatic one and has its place for examining the climate where
 95 the time scales are of interest, prevents examining the temporal evolution of the residual-
 96 mean fields and conflates temporal variability with the eddies. The conflation can have
 97 leading-order consequences in quantifying the energy cycle; by adjusting the temporal
 98 mean from monthly to annual, Aiki and Richards (2008, cf. Table 2 in their paper) show
 99 that the amount of kinetic and potential energy stored in the mean and eddy reservoirs
 100 can change by up to a factor of four. Eddy-mean flow interaction in the TWA frame-
 101 work, hence, warrants further investigation, and we believe our study is the first to strictly
 102 implement an ensemble mean in this context. In sections 4.1 and 4.2, we show that the
 103 ensemble framework provides new insights into turbulence studies.

104 When discussing *eddy* versus *mean flow*, one of the ambiguities lies in how the two
 105 are decomposed and interpreted (Bachman et al., 2015). As noted above, often, the ed-
 106 dies are defined from a practical standpoint as the deviation from a temporally and/or
 107 spatially coarse-grained field regardless of the coordinate system (e.g. Aiki & Richards,
 108 2008; Lévy et al., 2012; Sasaki et al., 2014; Griffies et al., 2015; Aoki et al., 2016; Uchida
 109 et al., 2017; Zhao & Marshall, 2020), which leaves open the question of how the filter-
 110 ing affects the decomposition. Due to the ensemble averaging nature of the TWA frame-
 111 work, we are able to uniquely define the two; the *mean flow* (ensemble mean) is the oceanic
 112 response to the surface boundary state and lateral boundary conditions, and the *eddy*
 113 (fluctuations about the ensemble mean) is the field due to intrinsic variability includ-
 114 ing mesoscale turbulence (Sérazin et al., 2017; Leroux et al., 2018).

115 The paper is organized as follows: We describe the model configuration in section 2
 116 and briefly provide an overview of the TWA framework in section 3. The results are given
 117 in section 4. In particular, our dataset provides a unique opportunity to examine the va-
 118 lidity of the often assumed ergodicity when decomposing the flow into its eddy and mean
 119 flow components, which we give in section 4.2. Discussion and conclusions are given in
 120 section 5.

121 2 Model description

122 We use the model outputs from the realistic runs described in Jamet et al. (2019b),
 123 Jamet et al. (2020) and Uchida, Jamet, et al. (2021), which are an air-sea partially cou-
 124 pled, 48-member ensemble of the North Atlantic ocean at mesoscale-permitting resolu-
 125 tion ($1/12^\circ$; or sometimes referred to as ‘eddy rich’) using the hydrostatic configuration
 126 of the Massachusetts Institute of Technology general circulation model (MITgcm; J. Mar-
 127 shall et al., 1997). We have 46 vertical levels increasing from 6 m near the surface to 250 m
 128 at depth. Harmonic, biharmonic horizontal and vertical viscosity values of $A_{h2} = 20 \text{ m}^2 \text{ s}^{-1}$,
 129 $A_{h4} = 10^{10} \text{ m}^4 \text{ s}^{-1}$ and $A_v = 10^{-5} \text{ m}^2 \text{ s}^{-1}$ were used respectively. For completeness,
 130 we provide a brief summary of the configuration below.

131 Figure 1 shows the bathymetry of the modelled domain extending from 20°S to 55°N .
 132 In order to save computational time and memory allocation, the North Atlantic basin
 133 was configured to zonally wrap around periodically. Open boundary conditions are ap-
 134 plied at the north and south boundaries of our domain and Strait of Gibraltar, such that
 135 oceanic velocities (\mathbf{u}) and potential temperature and practical salinity (Θ, S) are restored
 136 with a 36 minutes relaxation time scale toward a state derived by an ocean-only global
 137 Nucleus for European Modelling of the Ocean (NEMO) simulation (Molines et al., 2014,
 138 ORCA12.L46-MJM88 run in their paper, hereon referred to as ORCA12). The open bound-
 139 ary conditions are prescribed every five days from the ORCA12 run and linearly inter-
 140 polated in between. A sponge layer is further applied to two adjacent grid points from
 141 the open boundaries where model variables are restored toward boundary conditions with
 142 a one-day relaxation time scale. In total, relaxation is applied along three grid points
 143 from the boundaries with it being the strongest at the boundary along with radiation
 144 conditions at the northern/southern most boundary. Although relatively short, no ad-
 145 verse effects were apparent upon inspection in response to these relaxation time scales;
 146 e.g. changes in the open boundary conditions were seen to induce a physically consis-

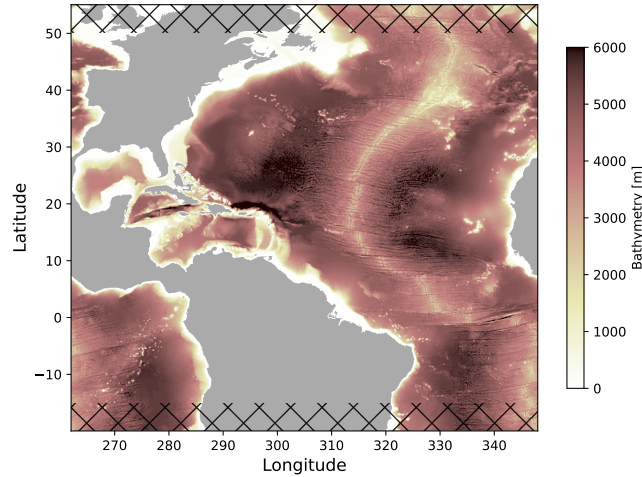


Figure 1. Bathymetry of the modelled domain. The domain was configured to wrap around zonally in order to save computation and memory allocation when generating the ensemble. The hatches indicate the northern and southern regions excluded from our analysis.

147 tent Atlantic Meridional Overturning Circulation response inside the domain (Jamet et
 148 al., 2020).

149 The 48-member ensemble was constructed as follows: 48 oceanic states separated
 150 by 48 hours each were taken during an initial 96-day-long integration beginning Novem-
 151 ber 14, 1962. Simulations initialized with these states were then run under yearly *repeat-*
 152 *ing* 1963 atmospheric and boundary conditions for a year, i.e. the atmospheric state and
 153 boundary conditions are cyclic for this year. After the one year of integration from the
 154 48 states, the last time step from each simulation was taken as the initial condition for
 155 the ensuing ensemble members; each spun-up initial oceanic state is physically consis-
 156 tent with the atmospheric and boundary conditions of January 1, 1963 (details are given
 157 in Jamet et al., 2020). At the surface, the ocean is partially coupled to an atmospheric
 158 boundary layer model (CheapAML; Deremble et al., 2013). In CheapAML, atmospheric
 159 surface temperature and relative humidity respond to ocean surface structures by ex-
 160 changes of heat and humidity computed according to the Coupled Ocean–Atmosphere
 161 Response Experiment (COARE3; Fairall et al., 2003) flux formula, but are strongly re-
 162 stored toward prescribed values over land; there are no zonally propagating signals of
 163 climate teleconnection. The prescribed atmospheric state is taken from the Drakkar forc-
 164 ing set and boundary forcing from the ORCA12 run (details are given in Jamet et al.,
 165 2019a). The ensemble members are integrated forward in time for 5 years (1963–1967),

166 and exposed to the same prescribed atmospheric state above the boundary layer and re-
 167 laxation at the north/south boundaries across all ensemble members. (Note that the forc-
 168 ing and relaxation are no longer cyclic after the one-year spin-up phase.) During this in-
 169 terval, the oceanic state and the atmospheric boundary layer temperature and humid-
 170 ity evolve in time. In the following, we interpret the ensemble mean as the ocean response
 171 to the atmospheric state prescribed above the atmospheric boundary layer as well as the
 172 oceanic conditions imposed at the open boundaries of the regional domain, while the en-
 173 semble spread is attributed to intrinsic ocean dynamics that develop at mesoscale-permitting
 174 resolution (S erazin et al., 2017; Leroux et al., 2018; Jamet et al., 2019b).

175 The model outputs were saved as five-day averages. In the context of mesoscale dy-
 176 namics, which is the focus of this study, some temporal averaging is appropriate in or-
 177 der to filter out temporal scales shorter than the mesoscale eddies themselves. From a
 178 probabilistic perspective, the five-day averaging results in more Gaussian-like eddy statis-
 179 tics (based on the central-limit theorem). From a dynamical point of view, this does not
 180 allow us to close the residual-mean and eddy budgets (cf. Stanley, 2018, Section 4.4).
 181 Nevertheless, the ensemble dimension of our dataset provides an unique opportunity to
 182 examine the TWA eddy-mean flow interaction. In the following analysis, we exclude the
 183 northern and southern extent of 5° from our analysis to avoid effects from the open bound-
 184 ary conditions and sponge layer (Figure 1) and to maximize the signal of intrinsic vari-
 185 ability amongst the ensemble members. We also use the last year of output (1967) for
 186 the same reasons.

187 **3 Theory and implementation of thickness-weighted averaging**

188 The ocean is a stratified fluid, and the circulation and advection of tracers tend to
 189 align themselves along the stratified density surfaces. Hence, a natural way to under-
 190 stand the circulation is to consider the variables in a buoyancy framework and the residual-
 191 mean flow rather than the Eulerian mean flow. We leave the detailed derivation of the
 192 TWA framework to Young (2012, and references therein) and here, only provide a brief
 193 summary; the primitive equations in geopotential coordinates are first transformed to
 194 buoyancy coordinates upon which a thickness weighting and ensemble averaging along
 195 constant buoyancy surfaces are applied to obtain the TWA governing equations. Follow-
 196 ing the notation by Young (2012) and Ringler et al. (2017), the TWA horizontal momen-

197 tum equations in the buoyancy coordinate system $(\tilde{t}, \tilde{x}, \tilde{y}, \tilde{b})$ are:

$$198 \quad \hat{u}_{\tilde{t}} + \hat{u}\hat{u}_{\tilde{x}} + \hat{v}\hat{u}_{\tilde{y}} + \hat{\omega}\hat{u}_{\tilde{b}} - f\hat{v} + \overline{m}_{\tilde{x}} = -\bar{\mathbf{e}}_1 \cdot (\tilde{\nabla} \cdot \mathbf{E}) + \hat{\mathcal{X}} \quad (1)$$

$$199 \quad \hat{v}_{\tilde{t}} + \hat{u}\hat{v}_{\tilde{x}} + \hat{v}\hat{v}_{\tilde{y}} + \hat{\omega}\hat{v}_{\tilde{b}} + f\hat{u} + \overline{m}_{\tilde{y}} = -\bar{\mathbf{e}}_2 \cdot (\tilde{\nabla} \cdot \mathbf{E}) + \hat{\mathcal{Y}} \quad (2)$$

201 where $\overline{(\cdot)}$ and $\widehat{(\cdot)} \stackrel{\text{def}}{=} \overline{\sigma^{-1} \sigma(\cdot)}$ are the ensemble averaged and TWA variables respectively,
 202 $\sigma (= \zeta_{\tilde{b}})$ the specific thickness and ζ the depth of an iso-surface of buoyancy. The sub-
 203 scripts denote partial derivatives. The Montgomery potential is $m = \check{\phi} - \tilde{b}\zeta$ where $\check{\phi}$
 204 is the dynamically active part of hydrostatic pressure (the meaning of $\check{(\cdot)}$ will become
 205 clearer later). ϖ is the dia-surface velocity across buoyancy contours, which we detail
 206 below for a realistic equation of state (EOS) for density. The vectors $\bar{\mathbf{e}}_1 = \mathbf{i} + \bar{\zeta}_{\tilde{x}} \mathbf{k}$ and
 207 $\bar{\mathbf{e}}_2 = \mathbf{j} + \bar{\zeta}_{\tilde{y}} \mathbf{k}$ form the basis vectors spanning the buoyancy horizontal space where \mathbf{i}, \mathbf{j}
 208 and \mathbf{k} are the Cartesian geopotential unit vectors, and \mathbf{E} is the E-P flux tensor described
 209 in detail in Section 4.1. Although each ensemble member has an individual basis $(\mathbf{e}_1, \mathbf{e}_2)$,
 210 the E-P flux divergence yields no cross terms upon averaging as the TWA operator com-
 211 mutes with the divergence of \mathbf{E} (for mathematical details, see Section 3.4 in Maddison
 212 & Marshall, 2013); this allows for the tensor expression in equations (1) and (2). \mathcal{X} and
 213 \mathcal{Y} are the viscous and forcing terms.

214 One subtle yet important point involves the buoyancy coordinate (\tilde{b}) for a realis-
 215 tic, non-linear EOS (Jackett & McDougall, 1995). The analysis in Young (2012) implic-
 216 itly assumes a linear EOS. With a realistic EOS, defining the vertical coordinate using
 217 potential density introduces errors. However, what constitutes a better buoyancy vari-
 218 able is the subject of some debate (e.g. Jackett & McDougall, 1997; McDougall & Jack-
 219 ett, 2005; de Szoek & Springer, 2009; Klocker et al., 2009; Tailleux, 2016; Lang et al.,
 220 2020). Although other choices are possible, we argue for the use of in-situ density *anomaly*
 221 ($\delta \stackrel{\text{def}}{=} \rho - \check{\rho}(z)$ where ρ is the in-situ density and $\check{\rho}$ is a function of only depth; Mont-
 222 gomery, 1937; Stanley, 2018, 2019). With in-situ density anomaly, buoyancy can be de-
 223 fined as:

$$224 \quad \underset{\sim}{b}(\Theta, S, z) \stackrel{\text{def}}{=} -\frac{g}{\rho_0} \delta \stackrel{\text{def}}{=} \tilde{b}(t, x, y, z) \quad (3)$$

225 where $\rho_0 = 999.8 \text{ kg m}^{-3}$ the Boussinesq reference density prescribed in MITgcm. $\underset{\sim}{b}$ is
 226 used to denote a thermodynamic function and \tilde{b} denotes the buoyancy at a point in space-time.
 227 The question becomes how to choose $\check{\rho}(z)$ so that monotonicity is maintained $\left(\left[\underset{\sim}{b} \right]_{\Theta, S} > \right.$
 228 0 ; the vertical partial derivative is taken in respect to constant potential temperature
 229 and practical salinity $([\cdot]_{\Theta, S})$. $\left[\frac{\partial}{\partial z} \underset{\sim}{b}(\Theta, S, z) \right]_{\Theta, S} > 0$ implies $\frac{\partial}{\partial z} \tilde{b}(t, x, y, z) > 0$ if the

230 stratification is statically stable). The vertical derivative of the in-situ density anomaly
 231 can be decomposed as:

$$232 \quad [\delta_z]_{\Theta,S} = [\rho_z]_{\Theta,S} - \frac{d}{dz} \check{\rho} = [\rho_{\Phi}]_{\Theta,S} \frac{d\Phi}{dz} - \frac{d}{dz} \check{\rho} = \frac{-\rho_0 g}{c_s^2} - \frac{d}{dz} \check{\rho}, \quad (4)$$

233 where $\Phi = -\rho_0 g z$ is the dynamically non-active part of hydrostatic pressure, and c_s
 234 is the sound speed. We remind the reader that a Boussinesq fluid is not strictly incom-
 235 compressible and a finite sound speed can be diagnosed (Olbers et al., 2012; Vallis, 2017).
 236 For simplicity, we can write $\frac{d}{dz} \check{\rho} \stackrel{\text{def}}{=} -\rho_0 g \mathcal{C}_s^{-2}$ where $\mathcal{C}_s = \mathcal{C}_s(z)$ is a function of only
 237 depth, which yields:

$$238 \quad \left[\underset{\sim}{b} \right]_{\Theta,S} = -\frac{g}{\rho_0} [\delta_z]_{\Theta,S} = g^2 \frac{\mathcal{C}_s^2 - c_s^2}{c_s^2 \mathcal{C}_s^2}. \quad (5)$$

239 Denoting $\mathcal{C}_s = c_s + \Delta_c$ where $c_s^{-1} \Delta_c \ll 1$, the right-hand side (RHS) of equation (5)
 240 becomes:

$$241 \quad g^2 \frac{(c_s + \Delta_c)^2 - c_s^2}{c_s^2 \mathcal{C}_s^2} \approx \frac{g^2}{\mathcal{C}_s^2} \left[\left(1 + \frac{2\Delta_c}{c_s} \right) - 1 \right] = \frac{2g^2 \Delta_c}{c_s \mathcal{C}_s^2} \sim O(10^{-6}). \quad (6)$$

242 Hence, so long as $\mathcal{C}_s \gtrsim c_s$, monotonicity is assured while removing a large portion of
 243 compressibility, i.e. the iso-surfaces of $\underset{\sim}{b}$ become close to neutral surfaces. In practice,
 244 we chose \mathcal{C}_s to be larger than the maximum sound speed at each depth by 10^{-5} m s^{-1}
 245 over the entire ensemble in order to avoid a singularity (viz. $\left[\underset{\sim}{b} \right]_{\Theta,S} = 0$). With \mathcal{C}_s
 246 determined, integrating for $\check{\rho}$ gives:

$$247 \quad \check{\rho} = - \int_z^0 \frac{\rho_0 g}{\mathcal{C}_s} dz + \rho_0, \quad (7)$$

248 which reduces to $\check{\rho}|_{z=0} = \rho_0$. The buoyancy equation using the in-situ density anomaly
 249 becomes:

$$250 \quad \frac{D}{Dt} \underset{\sim}{b} = \underset{\sim}{b} \underset{\sim}{\Theta} \dot{\Theta} + \underset{\sim}{b} \underset{\sim}{S} \dot{S} + \underset{\sim}{b} \frac{Dz}{Dt} \quad (8)$$

$$251 \quad = \mathcal{B} + wg^2 \frac{\mathcal{C}_s^2 - c_s^2}{c_s^2 \mathcal{C}_s^2}, \quad (9)$$

252 where $\mathcal{B} \stackrel{\text{def}}{=} \underset{\sim}{b} \underset{\sim}{\Theta} \dot{\Theta} + \underset{\sim}{b} \underset{\sim}{S} \dot{S}$, and $\dot{\Theta}$ and \dot{S} are the net diabatic contributions on potential
 253 temperature and practical salinity respectively, which we approximate by diagnosing off-
 254 line the sum of harmonic and biharmonic diffusion below the mixed layer using the five-
 255 day averaged outputs of Θ and S . We summarize the RHS of (9) as the dia-surface ve-
 256 locity $\varpi \stackrel{\text{def}}{=} \mathcal{B} + wg^2 \frac{\mathcal{C}_s^2 - c_s^2}{c_s^2 \mathcal{C}_s^2}$.

258 A further requirement of the TWA framework is that the pressure anomaly defined
 259 by such buoyancy coordinate translates into a body force in the buoyancy coordinate

$$260 \quad \nabla_{\text{h}} \check{\rho}(z) \mapsto \nabla_{\text{h}} \check{\rho}(\tilde{b}) = \tilde{\nabla}_{\text{h}} m, \quad (10)$$

261 where the subscript $(\cdot)_h$ represents the horizontal gradient and $\tilde{\nabla}_h = (\partial_{\tilde{x}}, \partial_{\tilde{y}})$. Using
 262 in-situ buoyancy anomaly, the pressure anomaly becomes:

$$263 \quad \check{\phi}(z) = \int_{\tilde{z}} b \, dz. \quad (11)$$

264 The $(\check{\cdot})$ is used to denote that the pressure anomaly is defined by the in-situ buoyancy
 265 anomaly. The pressure anomaly for a Boussinesq hydrostatic fluid, on the other hand,
 266 is:

$$267 \quad \phi(z) = \int -\frac{g}{\rho_0}(\rho - \rho_0) \, dz. \quad (12)$$

268 Since $\check{\rho}$ is only a function of depth, the horizontal gradient of the two remain identical
 269 ($\nabla_h \check{\phi} = \nabla_h \phi$) and equation (10) holds. (We note that equation (10) does not hold for
 270 pressure anomaly defined by potential density when the EOS is non-linear, and while
 271 more elaborate techniques may improve the neutrality of δ , the relation to the dynam-
 272 ics is non-trivial for other density variables such as neutral and orthobaric densities.) The
 273 use of in-situ density anomaly to define the buoyancy coordinate maintains the desir-
 274 able properties of a unique, statically stable vertical coordinate and a simple hydrostatic
 275 balance ($\sigma = \zeta_{\tilde{b}} = -m_{\tilde{b}\tilde{b}}$) while removing roughly 99% of the effect of compressibility
 276 basin wide at each depth ($\frac{g^2(c_s^{-2} - C_s^{-2})}{g^2 c_s^{-2}} \approx \frac{2c_s \Delta c}{c_s^2} \sim O(10^{-2})$). For a non-linear EOS, a
 277 material conservation of potential vorticity (PV) and non-acceleration conditions do not
 278 exist (cf. Vallis, 2017, Chapter 4). Discussion regarding the energetics are given in Ap-
 279 pendix A.

280 The raw simulation outputs were in geopotential coordinates so we first remapped
 281 all of the variables in equations (1) and (2) onto 55 buoyancy levels spread across the
 282 range of $\tilde{b} \in (-0.196, -0.287) \text{ m s}^{-2}$ (with the mathematical formulation of $\delta = \delta_0 +$
 283 $A_\delta \frac{\tanh(\tau) - \tanh(0)}{\tanh(\tau_{\max}) - \tanh(0)}$ where $\delta_0 = 20 \text{ kg m}^{-3}$, $A_\delta = 9.2 \text{ kg m}^{-3}$, and $\tau \in [0, 2)$ in order
 284 to account for the abyssal weak stratification):

$$285 \quad (u, v, b, \nabla_h \check{\phi}, \Theta, S, \varpi)(t, x, y, z) \mapsto (u, v, \zeta, \tilde{\nabla}_h m, \Theta, S, \varpi)(\tilde{t}, \tilde{x}, \tilde{y}, \tilde{b}) \quad (13)$$

286 using the `fastjmd95` Python package to compute the in-situ density and its partial deriva-
 287 tives (Abernathey, 2020), and the `xgcm` Python package (Abernathey et al., 2021; Jones
 288 et al., 2020; Busecke & Abernathey, 2020) which allows for coordinate remapping con-
 289 sistent with the finite-volume discretization of MITgcm. The horizontal velocity vector
 290 becomes $u\mathbf{i} + v\mathbf{j} \mapsto u\mathbf{e}_1 + v\mathbf{e}_2$. For the horizontal pressure anomaly gradient, we re-
 291 computed the pressure anomaly using the five-day averaged outputs and have invoked
 292 the identity (10). In the case where the buoyancy contour outcrops for some members,

293 we treat it by making the layer thickness vanish ($\Delta\zeta = 0$) and carry on with our TWA
 294 analysis. This is consistent with the boundary treatment of Young (2012) where he notes
 295 that buoyancy contours intersecting the boundary to be continued just beneath the sur-
 296 face.

297 4 Results

298 We start by showing the time series of domain-averaged horizontal kinetic energy
 299 (KE) and potential temperature, and an arbitrary buoyancy iso-surface (Figure 2). Fig-
 300 ure 2a shows the simulation has a prominent seasonal cycle with the KE and temper-
 301 ature both peaking in summer. In Figure 2, we also show the residual-mean fields on Jan-
 302 uary 3, 1967, the first day of the year of output we analyze. The depth of the buoyancy
 303 level shown in Figure 2c is below the ensemble-mean mixed-layer depth (MLD; Figure 2b)
 304 basin wide where diabatic effects are small, but is shallow enough to capture the imprint
 305 of the Gulf Stream; the iso-surface shoals drastically across the latitude of $\sim 38^\circ\text{N}$ where
 306 the separated Gulf Stream is situated (Figure 2d). The ensemble-mean MLD was com-
 307 puted as the depth at which the potential density computed from ensemble-mean tem-
 308 perature and salinity fields increased by 0.03 kg m^{-3} from the density at 10 m depth ($\overline{\text{MLD}} \stackrel{\text{def}}{=} \text{MLD}(\overline{\Theta}, \overline{S})$; de Boyer Montégut et al., 2004). The residual-mean KE field (MKE, $K^\# \stackrel{\text{def}}{=} |\hat{\mathbf{u}}|^2/2$; Figure 2d) shows the characteristic features of the Gulf Stream, North Brazil Cur-
 311 rent and equatorial undercurrent. The North Brazil Current, although having large val-
 312 ues in KE, shows no imprint on the buoyancy depth (Figure 2c). The residual-mean Rossby
 313 number ($\text{Ro}^\# \stackrel{\text{def}}{=} f^{-1}(\hat{v}_{\hat{x}} - \hat{u}_{\hat{y}})$) is smaller than unity over most of the Atlantic basin
 314 (Figure 2e), indicating that the residual-mean flow in the interior is balanced in our model
 315 with the exception of regions with energetic currents, e.g. the Gulf Stream, loop current
 316 in the Gulf of Mexico and the North Brazil Current. Near the equator, the Coriolis pa-
 317 rameter becomes small leading to large Rossby numbers. The kinematics of discretiz-
 318 ing the gradients in buoyancy coordinates are given in Appendix B. We now move on
 319 to examine the eddy feedback onto the (residual) mean flow. Hereon, we drop the pre-
 320 fix ‘residual’ unless required for clarity.

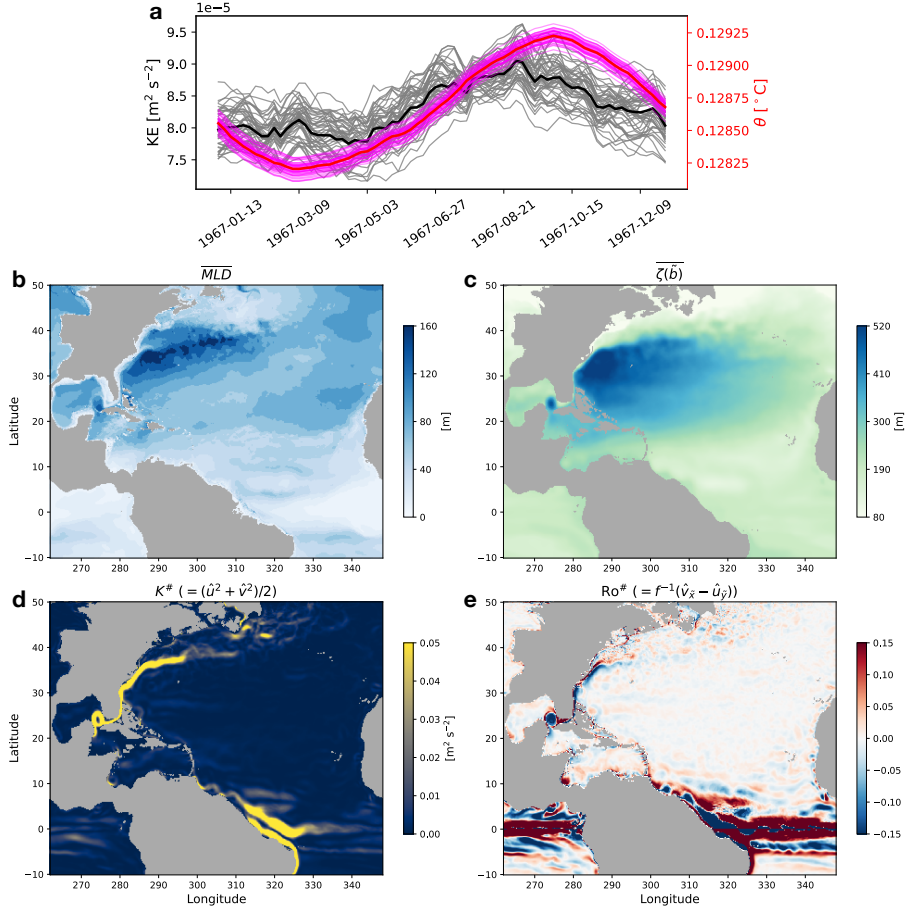


Figure 2. Time series of the domain-averaged total KE (black) and potential temperature (red) for the 48 ensemble members between 15°S-50°N. The thick lines show the ensemble mean and the thin lines each ensemble member **a**. The ensemble-mean MLD on January 3, 1967 and depth of the iso-surface of buoyancy $\tilde{b} = -0.26 \text{ m s}^{-2}$ **b,c**. The residual-mean KE ($K^{\#}$) and Rossby number ($\text{Ro}^{\#}$) on the same buoyancy surface **d,e**.

321

4.1 The Eliassen-Palm flux

322

The E-P flux tensor (\mathbf{E}) in the TWA framework (equations (1) and (2)) is:

$$\mathbf{E} = \begin{pmatrix} \widehat{u''u''} + \frac{1}{2\bar{\sigma}}\overline{\zeta'^2} & \widehat{u''v''} & 0 \\ \widehat{v''u''} & \widehat{v''v''} + \frac{1}{2\bar{\sigma}}\overline{\zeta'^2} & 0 \\ \overline{\varpi''u''} + \frac{1}{\bar{\sigma}}\overline{\zeta'm'_x} & \overline{\varpi''v''} + \frac{1}{\bar{\sigma}}\overline{\zeta'm'_y} & 0 \end{pmatrix} \quad (14)$$

324

325

326

327

where $(\cdot)'' = (\cdot) - \widehat{(\cdot)}$ and $(\cdot)' = (\cdot) - \overline{(\cdot)}$ are the residual from the thickness-weighted and ensemble averages respectively (Maddison & Marshall, 2013; Aoki, 2014; Ringler et al., 2017). The two are related via the (eddy-induced) bolus velocity (Greatbatch, 1998; McDougall & McIntosh, 2001):

328

$$\mathbf{u}'' = \mathbf{u} - \frac{\bar{\sigma}\bar{\mathbf{u}}}{\bar{\sigma}} = \bar{\mathbf{u}} + \mathbf{u}' - \frac{(\bar{\sigma} + \sigma')(\bar{\mathbf{u}} + \mathbf{u}')}{\bar{\sigma}} \quad (15)$$

329

330

$$= \mathbf{u}' + \frac{\sigma'\mathbf{u}'}{\bar{\sigma}}. \quad (16)$$

331

332

333

334

335

336

337

338

339

340

341

342

343

344

345

346

347

348

We show each term in equation (14) in Figure 3. The eddy momentum flux $\widehat{u''v''}$ is often associated with barotropic processes in analogy to atmospheric jets (Figure 3a; Chan et al., 2007; Aoki et al., 2016; Jamet et al., 2021; Vallis, 2017, Chapter 15). The zonal and meridional eddy momentum flux $(\widehat{u''^2}, \widehat{v''^2})$ exchange momentum between the eddies and mean flow, i.e. to accelerate or decelerate the Gulf Stream as they affect the horizontal shear upon taking their gradients. The term due to the vertical displacement of buoyancy layer $(\frac{1}{2\bar{\sigma}}\overline{\zeta'^2})$ is related to the eddy potential energy (EPE; cf. equations A15-A17). The interfacial form stress $(\overline{\zeta'\tilde{\nabla}_h m'})$; Figure 3e,f) often associated with baroclinic instability is “deceivingly” orders of magnitude smaller than the other terms. However, it is the divergence of the E-P flux and not the flux itself that goes into the momentum equations, and the horizontal $(\tilde{\nabla}_h)$ and vertical gradient $(\partial_{\tilde{z}})$ differ by roughly $O(10^6)$. The contribution from the diabatic and compressibility effects (i.e. the terms with ϖ) were smaller than the interfacial form stress by another order of magnitude or more in the subtropics (not shown). It is quite surprising that the signals in the equatorial undercurrent region, although having relatively high KE (Figure 2d), are significantly smaller than in the Gulf Stream and North Brazil Current regions, virtually not visible in Figure 3. This implies that the mean flow dominates over the eddies in the equatorial region.

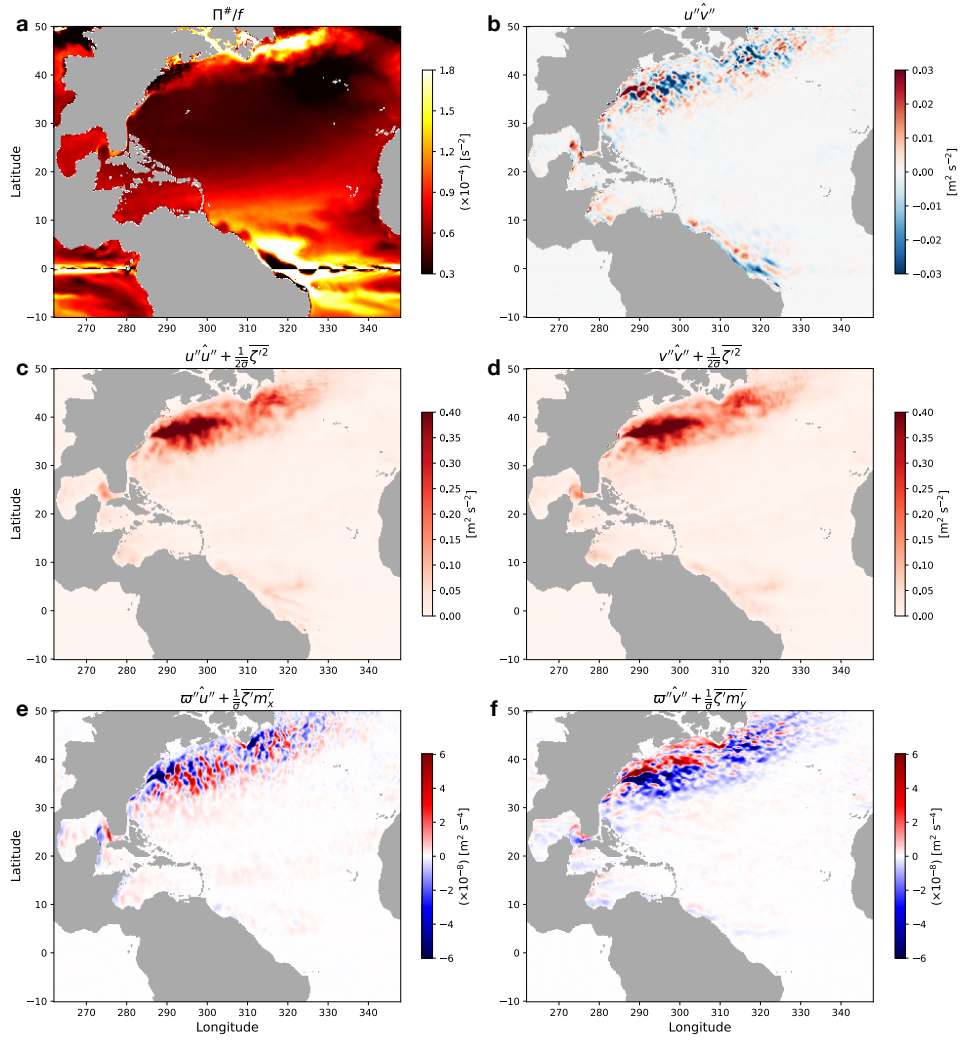


Figure 3. The residual-mean Ertel potential vorticity normalized by the local Coriolis parameter ($\Pi^\# / f \stackrel{\text{def}}{=} \bar{\sigma}^{-1}(1 + \text{Ro}^\#)$) **a** and terms in the E-P flux tensor **b-f** on January 3, 1967 on the iso-surface of buoyancy as in Figure 2. Note the scaling factors on panels a, e and f.

349 Writing out the E-P flux divergence in equations (1) and (2) gives:

$$350 \quad -\bar{\mathbf{e}}_1 \cdot (\tilde{\nabla} \cdot \mathbf{E}) = -\bar{\sigma}^{-1} \left([\overline{\sigma(u''u'')} + \frac{1}{2\bar{\sigma}} \overline{\zeta'^2}]_{\bar{x}} + [\overline{\sigma v''u''}]_{\bar{y}} + [\overline{\sigma(\varpi''u'' + \frac{1}{\bar{\sigma}} \overline{\zeta' m'_{\bar{x}}})}]_{\bar{b}} \right) \quad (17)$$

$$351 \quad = -\bar{\sigma}^{-1} \left([\overline{\sigma u''u''} + \overline{\zeta'^2}/2]_{\bar{x}} + [\overline{\sigma v''u''}]_{\bar{y}} + [\overline{\sigma \varpi''u''} + \overline{\zeta' m'_{\bar{x}}}]_{\bar{b}} \right), \quad (18)$$

$$352 \quad \stackrel{\text{def}}{=} -(E_{\bar{x}}^{00} + E_{\bar{y}}^{10} + E_{\bar{b}}^{20}) \quad (19)$$

$$353 \quad -\bar{\mathbf{e}}_2 \cdot (\tilde{\nabla} \cdot \mathbf{E}) = -\bar{\sigma}^{-1} \left([\overline{\sigma u''v''}]_{\bar{x}} + [\overline{\sigma(v''v'' + \frac{1}{2\bar{\sigma}} \overline{\zeta'^2})}]_{\bar{y}} + [\overline{\sigma(\varpi''v'' + \frac{1}{\bar{\sigma}} \overline{\zeta' m'_{\bar{y}}})}]_{\bar{b}} \right) \quad (20)$$

$$354 \quad = -\bar{\sigma}^{-1} \left([\overline{\sigma u''v''}]_{\bar{x}} + [\overline{\sigma v''v''} + \overline{\zeta'^2}/2]_{\bar{y}} + [\overline{\sigma \varpi''v''} + \overline{\zeta' m'_{\bar{y}}}]_{\bar{b}} \right), \quad (21)$$

$$355 \quad \stackrel{\text{def}}{=} -(E_{\bar{x}}^{01} + E_{\bar{y}}^{11} + E_{\bar{b}}^{21}). \quad (22)$$

359 As the signal in the North Atlantic basin is the largest in the separated Gulf Stream re-
 360 gion (Figure 3), we show each term in the E-P flux divergence north of 25°N (Figure 4).
 361 The large signal is consistent with Jamet et al. (2021) where they found the subtropi-
 362 cal gyre to be a Fofonoff-like inertial circulation (Fofonoff, 1981), and that the separated
 363 jet was where the energy input to the gyre from surface winds was predominantly lost
 364 to eddies. The convergence of interfacial form stress (E_b^{20}, E_b^{21}) becomes larger than the
 365 convergence of the eddy momentum flux terms due to cross correlation in the zonal and
 366 meridional momentum ($E_{\bar{y}}^{10}, E_{\bar{x}}^{01}$), which are the smallest amongst the three terms in the
 367 E-P flux convergence (Figure 4b,c). The contribution from the terms with dia-surface
 368 velocity (ϖ'') was roughly two-orders of magnitude smaller than the other terms in the
 369 E-P flux convergence in the adiabatic interior (not shown), which supports the neutral-
 370 ity of δ to define the buoyancy surfaces. Right at the separation of the Gulf Stream west
 371 of 290°E and around 36°N, the convergence of eddy momentum flux and potential en-
 372 ergy ($E_{\bar{x}}^{00}, E_{\bar{y}}^{11}$), and interfacial form stress (E_b^{20}, E_b^{21}) tend to counteract each other; in
 373 the zonal direction, the eddy momentum flux and potential energy convergence tends
 374 to decelerate the Gulf Stream while the interfacial form stress convergence tends to ac-
 375 celerate it (Figure 4a,e). The repeating positive and negative features further downstream
 376 are roughly on the scales of the Rossby deformation radius, consistent with Uchida, Derem-
 377 ble, Dewar, and Penduff (2021) where they diagnosed the E-P flux convergence from a
 378 101-member quasi-geostrophic (QG) double-gyre ensemble. In the meridional direction,
 379 the eddy momentum flux and potential energy convergence also tend to smooth out the
 380 Gulf Stream (decelerate the jet in the subpolar gyre by injecting northward momentum,
 381 and southward momentum in the subtropical gyre) while the interfacial form stress con-
 382 vergence tends to sharpen it (Figure 4d,f). The similar order of magnitude between $E_{\bar{x}}^{00}, E_{\bar{y}}^{11}$
 383 and E_b^{20}, E_b^{21} is in contrast, however, from a fully developed QG jet within a wind-driven

384 double-gyre circulation where the interfacial form stress convergence dominated the E-
 385 P flux convergence (Uchida, Deremble, Dewar, & Penduff, 2021). While this does not
 386 provide as proof that the Gulf Stream in primitive equation models deviates from quasi
 387 geostrophy, the disagreement is consistent with previous studies arguing that western
 388 boundary currents, which are on the order of $O(100\text{km})$ in the across-jet direction but
 389 $O(1000\text{km})$ in the along-jet direction, may not be well approximated by QG dynamics,
 390 which is isotropic in its formulation (Grooms et al., 2011; Jamet et al., 2021). Further
 391 examinations, however, are required to quantify the level of deviation.

392 We now examine further details in the separated Gulf Stream, a region where ed-
 393 dies have been shown to modulate the mean flow structure (e.g. Cronin, 1996; Chassignet
 394 & Xu, 2021), as seasonal means in order to capture representative features. Winter is
 395 defined as the months of January, February, March, and summer as July, August, Septem-
 396 ber. Upon separation, the zonal E-P flux convergence tends to decelerate the Gulf Stream.
 397 The repeating features of positive and negative values for the zonal component of the
 398 E-P flux convergence persist and are likely associated to the jet meandering (Figure 5a,c).
 399 In the meridional direction, we again see positive values on the northern flank of the sep-
 400 arated Gulf Stream and negative on its southern flank (Figure 5b,d). This north-south
 401 dipole feature is likely associated with the gradient of the eddy energy, and may be triv-
 402 ial as the energy naturally maximizes near the center of the jet. The zonal and merid-
 403 ional component of the E-P flux convergence can jointly be interpreted to force the Gulf
 404 Stream to migrate northwards (decelerate the jet northwards in the subtropical gyre on
 405 the North flank of the separated Gulf Stream and southwards in the subpolar gyre; Fig-
 406 ure 4b,d) although this largely being contained west of 310°E . The interpretation of pole-
 407 ward jet migration is consistent with the zonal E-P flux convergence where the overall
 408 structure of the forcing of the zonal equation is a deceleration on one side of the Gulf
 409 Stream and an acceleration on the other; the eddy momentum flux in the zonal momen-
 410 tum equation decelerate both the core and the flanks immediately downstream of Cape
 411 Hatteras (Figure 4a) and alternate further downstream (a signature of meandering) while
 412 the form drag term partially cancels this (Figure 4e). East of 310°E , the E-P flux con-
 413 vergence tends to shift the North Atlantic Current east and southwards in the open ocean,
 414 while northwards closer to the continental rise (Figure 4h). Examining the meridional
 415 transect averaged over the zonal extent of 290°E - 305°E where the separated Gulf Steam
 416 is roughly zonal (Figure 2d), the separated Gulf Stream can be identified with the steep

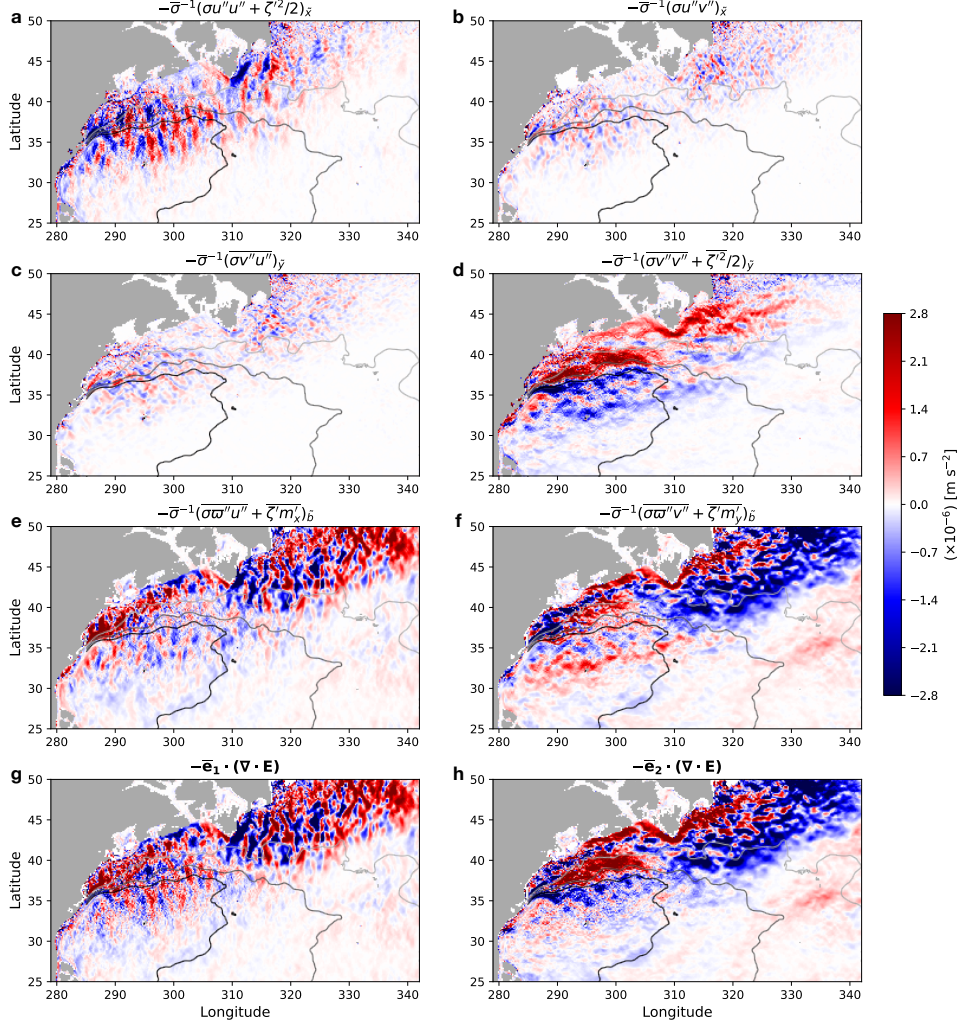


Figure 4. The terms in the convergence of E-P flux tensor on January 3, 1967 on the iso-surface of $\tilde{b} = -0.26 \text{ m s}^{-2}$ **a-f**. Positive values (red shadings) indicate the eddies fluxing momentum to the mean flow and vice versa. The panels are laid out so that summing up the top three rows per column yields the total zonal ($-\bar{\mathbf{e}}_1 \cdot (\tilde{\nabla} \cdot \mathbf{E})$) **g** and meridional E-P flux divergence ($-\bar{\mathbf{e}}_2 \cdot (\tilde{\nabla} \cdot \mathbf{E})$) **h** respectively. The contours in grey shading east of 285°E indicate the 400, 300 and 200 m depth of the buoyancy surface.

417 shoaling of the iso-surfaces of buoyancy between 36°N-40°N (Figure 5e-h). The overall
 418 magnitude and reversal in sign at the core of the jet (around 37.5°N) with diminishing
 419 amplitude with depth for the zonal E-P flux convergence during winter ($-\bar{\mathbf{e}}_1 \cdot (\tilde{\nabla} \cdot \mathbf{E})$;
 420 Figures 5g, 6a,b) is roughly in agreement with Ringler et al. (2017, their Figure 6 where
 421 the sign convention in equation (17) is reversed from ours for the eddy forcing term and
 422 their units are in $[\text{m s}^{-1} \text{ day}^{-1}]$) where they diagnosed an idealized zonally re-entrant
 423 jet. It is interesting to note, however, that the vertical structure of the E-P flux conver-
 424 gence is much smoother and barotropic during the summer with a consistent decelera-
 425 tion of the jet on its northern flank and acceleration on its southern flank (Figures 5g,
 426 6e,f). We note that such seasonal features may be specific to the year of 1967, and the
 427 temporal evolution of the E-P flux convergence should be addressed in a dedicated study.
 428 We leave this for further work, focusing here on the TWA implementation for a realis-
 429 tic model.

430 In Figure 6, we show the vertical profile of the seasonal E-P flux convergence along
 431 with each component in equations (17) and (20) area averaged over the zonal extent of
 432 290°E-305°E. The E-P flux convergence closely follows that of the interfacial form stress
 433 convergence (i.e. baroclinic instability) with the Reynolds stress due to cross correlation
 434 between the zonal and meridional eddy momentum (E_y^{10}, E_x^{01} ; orange lines) taking the
 435 smallest magnitude. The amplitude of interfacial form stress convergence is larger near
 436 the surface (viz. larger buoyancy values), which is expected from the seasonal surface
 437 forcing affecting the isopycnal tilt and hence baroclinicity of the surface flow. The merid-
 438 ional smoothing of the separated Gulf Stream is also apparent from the vertical profiles
 439 with the meridional E-P flux convergence taking negative values on the southern flank
 440 of the jet and positive values on the northern flank. The convergence of eddy momen-
 441 tum flux and potential energy tends to mirror that of interfacial form stress (blue and
 442 green lines in Figure 6). This counteracting balance is consistent with what Aoki et al.
 443 (2016, the terms $\partial_x R^x$ and $\partial_z(R^z + F_a^+)$ in their Figures 5a and 6) found in the Kuroshio
 444 extension region.

445 4.2 The ergodic assumption

446 In this section, we replace the averaging operator with the temporal mean of the
 447 50 years of output ($\overline{(\cdot)^t}, (\cdot)^t \stackrel{\text{def}}{=} (\cdot) - \overline{(\cdot)^t}$) from a single arbitrary realization (realiza-
 448 tion 00 to be specific) to examine the ergodic assumption and compare with our TWA

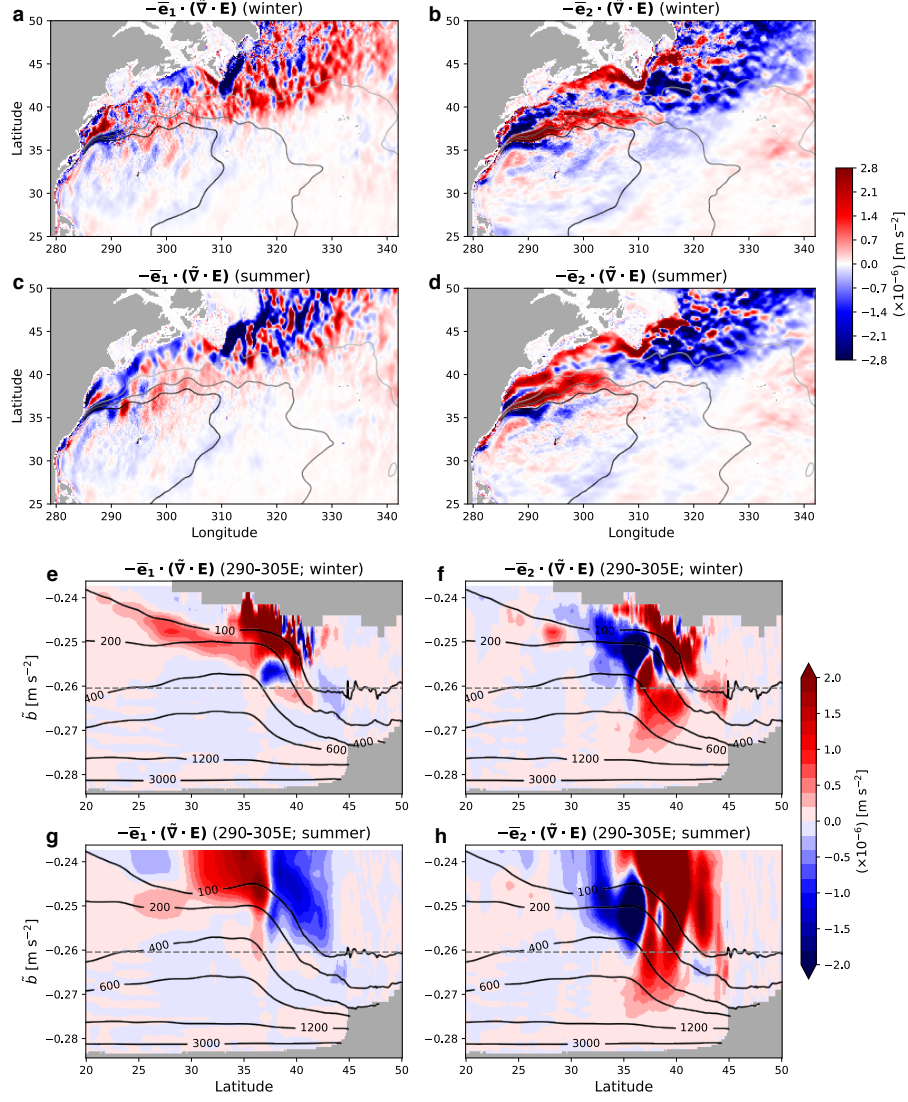


Figure 5. The seasonal mean of the zonal and meridional E-P flux convergence for winter and summer of 1967 **a-d**. The contours in grey shading indicate the 400, 300 and 200 m depth of the buoyancy surface. The zonal-mean transect between 290°E-305°E of the E-P flux convergence is shown in colored shading and ensemble-mean depth in black contours **e-h**. The iso-surface of buoyancy used through Figures 2-4 is shown as the grey dashed line. The masked out region north of 30°N near the surface during winter is where the iso-surfaces of buoyancy outcrop across all ensemble members. We see that more buoyancy surfaces outcrop during winter.

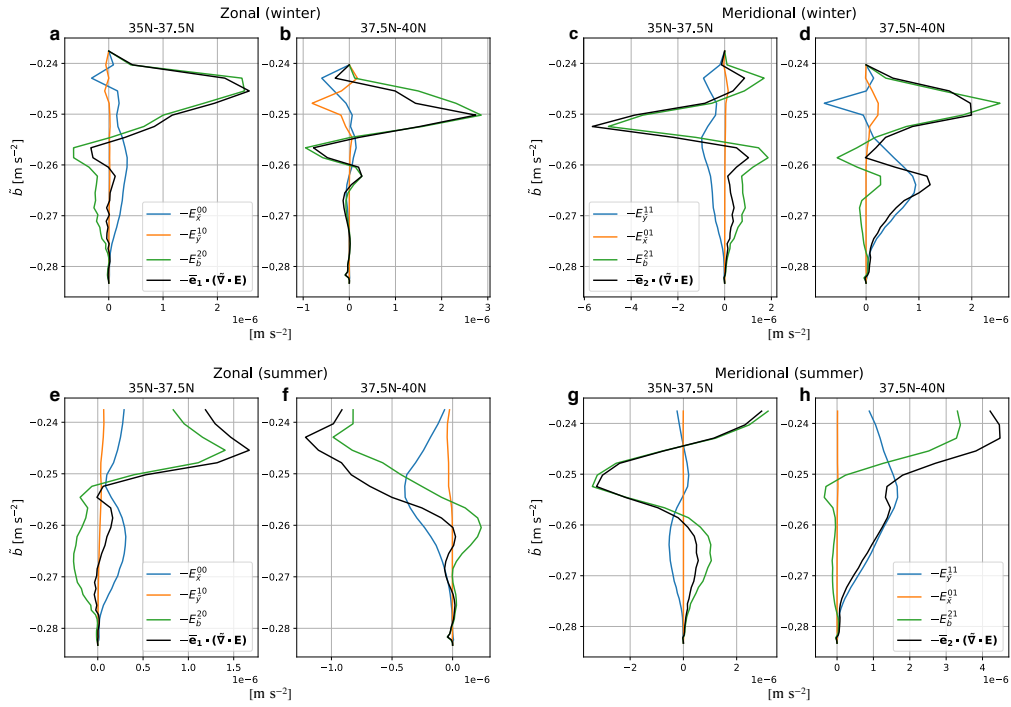


Figure 6. Vertical profile of the area-averaged, seasonal zonal and meridional E-P flux convergence north and south of the separated Gulf Stream over the zonal extent 290°E - 305°E . The area averaging is separated between 35°N - 37.5°N and 37.5°N - 40°N . The top panels show the seasonal mean for winter and bottom for summer.

449 results. Realization 00 was taken from a 24-member ensemble originally designed for a
 450 different study (Jamet et al., 2019b). The 48 members discussed above were constructed
 451 by adding 24 members to the first five years of this dataset. The TWA operator now be-
 452 comes $\widehat{(\cdot)}^t \stackrel{\text{def}}{=} \overline{\sigma^{t-1}(\cdot)}^t$ and eddies $(\cdot)''^t \stackrel{\text{def}}{=} (\cdot) - \widehat{(\cdot)}^t$. The maximum sound speed per
 453 depth (C_s) was recomputed for the 50 years of realization 00 in remapping the coordi-
 454 nate system. Although the averaging operator is now along the time dimension, we note
 455 that this is different from the Temporal-Residual Mean (TRM) framework developed by
 456 McDougall and McIntosh (2001) in the sense that we proceed with our analysis in buoy-
 457 ancy coordinate. The hope of applying the ergodic assumption to a temporally varying
 458 system, as we have shown in previous sections, is that for a sufficiently long time series,
 459 such sub- and inter-annual variability will cancel out with only the stationary feature
 460 being extracted in the ‘mean’ flow.

461 In Figure 7, we show the climatological E-P flux convergence from realization 00.
 462 In other words, all time scales shorter than 50 years are now relegated to the eddies. While
 463 having similar spatial structures to Figures 4 and 5a-d, they are more spread out with
 464 less detail. In particular, the seasonality is obscured by the climatological mean of 50
 465 years and becomes similar to the summertime of the 48-member ensemble (Figure 5c,d).
 466 In other words, the wintertime signal seen with the ensemble diagnostics (Figure 5a,b)
 467 are not well captured by the climatological E-P fluxes convergence. This could either sug-
 468 gest that such signal are peculiar to the year 1967 we analyzed with our 48-member en-
 469 semble, or that summertime signals may have a stronger imprint on the residual time
 470 mean. Considering the 50-year time scale of averaging, the signals that emerge in the
 471 climatological E-P flux convergence are likely due to transient eddies while the stand-
 472 ing eddies would be included in the mean flow. The climatological zonal-mean transect
 473 also resemble the ensemble summertime albeit with weaker amplitude (Figures 5e-h and
 474 8) where the eddies tend to zonally decelerate the separated Gulf Stream on its north-
 475 ern flank and accelerate it on its southern flank (Figure 8a). In the meridional direction,
 476 the eddies tend to decelerate the subpolar gyre on the northern flank of the separated
 477 Gulf Stream and the subtropical gyre on its southern flank (Figure 8b).

478 Taking the climatological time mean of 50 years of output is perhaps the most con-
 479 servative definition of the mean flow under ergodicity. We, therefore, now loosen the tem-
 480 poral averaging to a climatological annual cycle in defining the residual mean flow. In
 481 doing so, we chunk the 50 years into 50 annual segments and take their average to pro-

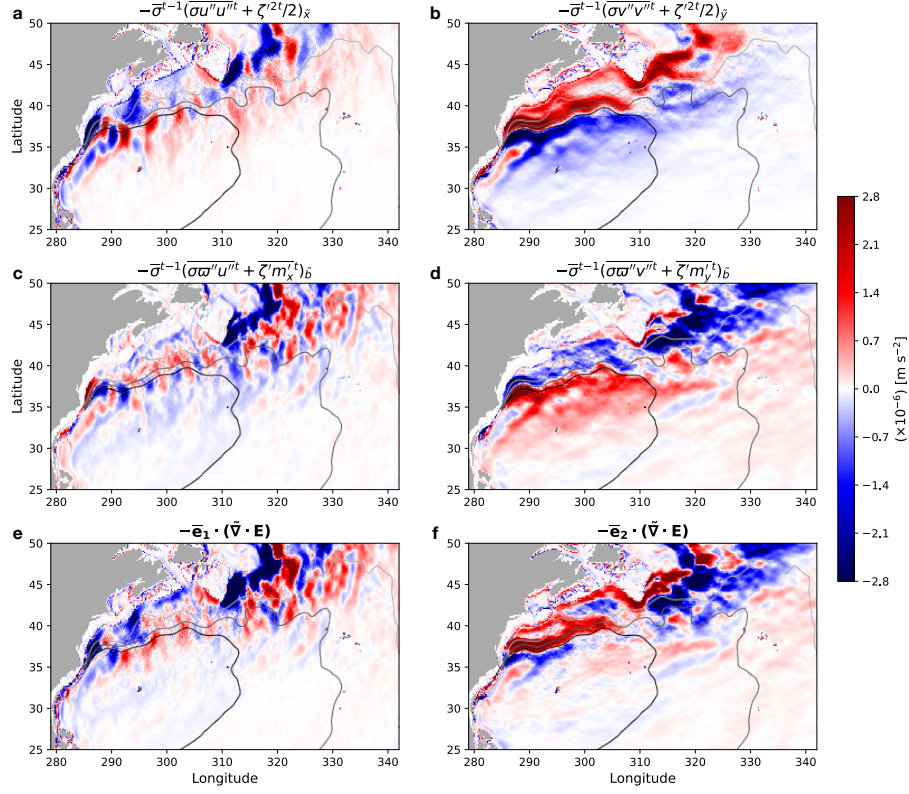


Figure 7. The terms in the climatological convergence of E-P flux tensor on the iso-surface of $\tilde{b} = -0.26 \text{ m s}^{-2}$ from realization 00 **a-d**. We do not show the terms due to the Reynolds stress ($\widehat{u''^t v''^t}$) as they were negligible compared to the other terms, and omit the superscript t on variables with primes to avoid the clutter. Climatology of the total zonal ($-\bar{\mathbf{e}}_1 \cdot (\tilde{\nabla} \cdot \mathbf{E})$) and meridional E-P flux divergence ($-\bar{\mathbf{e}}_2 \cdot (\tilde{\nabla} \cdot \mathbf{E})$) respectively **e,f**. The contours in grey shading east of 285°E indicate the 400, 300 and 200 m depth of the buoyancy surface.

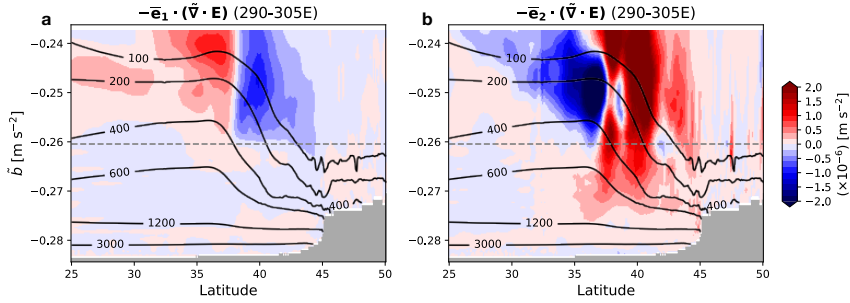


Figure 8. The climatological zonal-mean transect between 290°E - 305°E of the E-P flux convergence is shown in colored shading and ensemble-mean depth in black contours from realization 00 **a,b**. The iso-surface of buoyancy used in Figure 7 is shown as the grey dashed line.

482 duce a single segment of ~ 365 days. Namely, we treat each year as an individual re-
 483 realization of the ocean, generating a pseudo 50-member year-long ensemble (hereon pseudo-
 484 ensemble for short). The eddies are now defined as fluctuations about this climatolog-
 485 ical annual cycle. In Figure 9, we show the MKE on a buoyancy level on January 3 with
 486 similar depths diagnosed from the ensemble and pseudo-ensemble. While the maximum
 487 MKE amplitudes are similar, the mean flow is more spread out in the pseudo-ensemble.
 488 This likely comes from the different paths the Gulf Stream takes resulting as a response
 489 to different yearly atmospheric states, which get averaged all together. In other words,
 490 while the degrees of freedom are similar between the ensemble (48 members) and pseudo-
 491 ensemble (50 members assuming a decorrelation time scale of a year), the ensemble mean
 492 captures the oceanic response to the atmospheric state specific to 1967. The pseudo-ensemble,
 493 on the other hand, implies that 50 years are not sufficient for the ‘eddies’ to emerge as
 494 a coherent signal upon averaging for a climatological annual cycle and the mean flow in-
 495 corporates the signal of atmospheric interannual, decadal and low-frequency variability.

496 The imprint of fluctuations from each year onto the MKE domain averaged over
 497 the depths of $\sim 50\text{-}500$ m ($\tilde{b} \in (-0.25, -0.26)$) result in its seasonality to differ from the
 498 ensemble mean; the pseudo-ensemble takes its maximum around March while the ensem-
 499 ble around August (black solid and dashed lines in Figure 9c respectively). However, the
 500 seasonality in the area averaged MKE from the pseudo-ensemble on $\tilde{b} = -0.26$ shows
 501 a summertime maximum (black dot-dashed line in Figure 9c). This implies that the dis-
 502 crepancy between $K^\#$ and $K^{\#t}$ results from the surface ocean being sensitive to the at-
 503 mospheric state while being less so in the interior. Indeed, the domain averaged eddy
 504 KE (EKE; see Appendix A for definition) diagnosed from the ensemble shows a max-
 505 imum during winter when the surface ocean is more susceptible to baroclinic instabil-
 506 ity due to atmospheric cooling (red line in Figure 9c; Uchida et al., 2017). We conclude
 507 that in the process of creating a climatological annual cycle, we convolute the oceanic
 508 response to different atmospheric states (i.e. interannual variability) and contaminate
 509 the eddy-mean flow decomposition. The oceanic mean flow conflated with atmospheric
 510 variability also imprints itself onto the E-P flux convergence for the climatological win-
 511 ter and summer as we show in Figure 10, which arguably looks noisier than Figure 5a-
 512 d particularly north of the 300 m depth contour in the subpolar gyre.

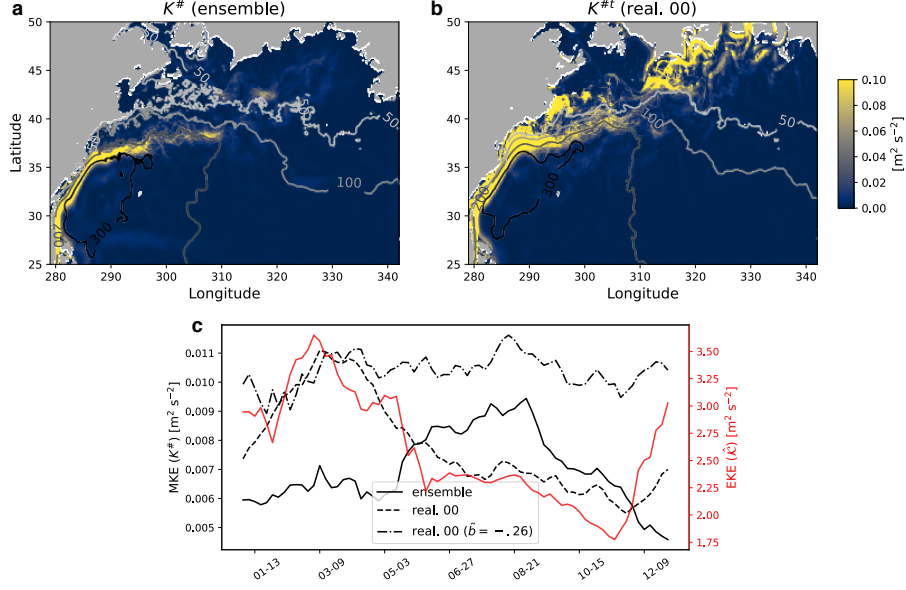


Figure 9. The (residual) mean KE on January 3 from the ensemble ($K^\#$) and pseudo-ensemble ($K^{\#t}$) on buoyancy levels with similar depth **a,b**. The regions with outcropping buoyancy surface are masked out. The colors indicate the MKE and contours in grey scaling show the depths for 50, 100, 200 and 300 m. Time series of domain averaged MKE ($K^\#$ and $K^{\#t}$) in black plotted against the left y axis and EKE ($\widehat{\mathcal{K}}$) in red plotted against the right y axis **c**. The domain was taken over the horizontal extent shown in panels a,b. Note the difference in magnitudes of order on the y axes.

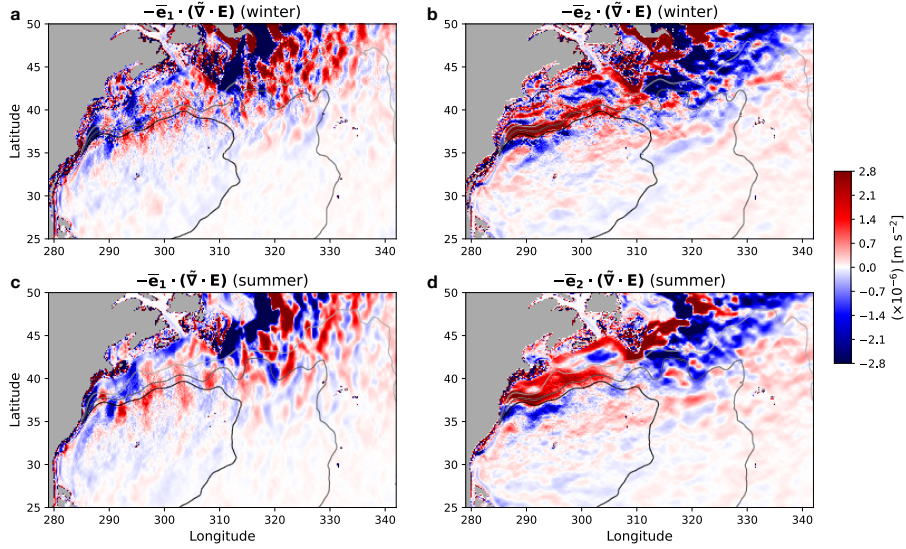


Figure 10. The E-P flux convergence from the pseudo-ensemble for the climatological winter and summer on the iso-surface of $\tilde{b} = -0.26 \text{ m} \cdot \text{s}^{-2}$. The contours in grey shading east of 285°E indicate the 400, 300 and 200 m depth of the buoyancy surface.

5 Discussion and summary

By running a 48-member ensemble run of the North Atlantic Ocean at mesoscale-permitting resolution ($1/12^\circ$) partially coupled to the atmosphere, we have shown that the thickness-weighted average (TWA) framework can be employed successfully in diagnosing eddy-mean flow interactions in a realistic ocean simulation. In doing so, we have introduced a new buoyancy variable for a realistic EOS, which is approximately neutral and dynamically consistent; both characteristics are necessary for the TWA analysis (Stanley, 2018). The ensemble approach negates the necessity for any temporal averaging in defining the residual-mean flow; we are able to exclude any temporal variability, such as seasonal and interannual fluctuations, from the eddy term and extract the intrinsic variability of the ocean. We show that the Eliassen-Palm (E-P) flux convergence (i.e. negative divergence), which encapsulates the eddy feedback onto the mean flow (Maddison & Marshall, 2013), tends to accelerate the Gulf Stream northwards on its northern flank ($-\bar{\mathbf{e}}_2 \cdot (\tilde{\nabla} \cdot \mathbf{E}) > 0$) and decelerate it on its southern flank ($-\bar{\mathbf{e}}_2 \cdot (\tilde{\nabla} \cdot \mathbf{E}) < 0$; Figure 5b,d,f,h); i.e. the eddies can be interpreted to force the Gulf Stream to migrate northwards on January 3, 1967. However, a more detailed examination of the mechanism of poleward jet migration will likely necessitate studies using idealized simulations where each dynamical mechanism is easier to parse out (cf. Chemke & Kaspi, 2015). Here, we have documented a dynamically-consistent implementation of the TWA framework for a realistic ocean simulation and the E-P flux convergence diagnosed in the context of oceanic ensemble simulations.

Modelling studies with varying spatial resolution have shown that the Gulf Stream tends to overshoot northwards and the North Atlantic Current (NAC) flows too zonally in coarse resolution models (e.g. Lévy et al., 2010; Chassignet & Xu, 2017, 2021). The overshooting may partially be attributable to eddy feedback being insufficiently resolved at mesoscale-permitting resolutions, in addition to unresolved submesoscale boundary layer processes (e.g. Renault et al., 2016). In particular, it would be interesting to see whether further increasing the model resolution would increase the amplitude of baroclinic instability near the surface (E_b^{20}, E_b^{21}) and convergence of eddy momentum flux and potential energy in the interior (E_x^{00}, E_y^{11}), which tend to accelerate the jet southward in the subpolar gyre and decelerate it southward in the subtropical gyre upon the Gulf Stream separation west of 290°E (i.e. shift the jet southwards) as we see from their annual means (Figure 11). The same could be said for a better representation of the NAC

546 path where the eddies in our model tend to flux northward momentum into the mean
 547 flow and hence allow for its north-eastward turn near the continental rise of the Grand
 548 Banks (Figures 4 and 5). Although it is beyond the scope of this study, the significance
 549 of baroclinic processes will likely increase with resolution as mixed-layer instability be-
 550 comes better resolved (Boccaletti et al., 2007; Capet et al., 2008a, 2008b; Su et al., 2018;
 551 Uchida et al., 2019; Yang et al., 2021).

552 We have also examined the often assumed ergodicity in decomposing the eddy and
 553 mean flow by replacing the averaging operator with a 50-year time mean for a single re-
 554 alization within the ensemble. To some extent, the agreement between Figures 4, 5, 11
 555 and 7 implies that the ensemble size of 48 is able to extract the eddy signals that emerge
 556 at mesoscale-permitting resolution. The difference between the ensemble and 50-year cli-
 557 matology of an arbitrary realization amongst the ensemble (realization 00), on the other
 558 hand, likely comes from seasonal, interannual and decadal variability, and transient ed-
 559 dies, which are obscured in the climatological view. Loosening the time mean to a cli-
 560 matological annual cycle for the mean flow, on the other hand, convolutes the oceanic
 561 response to interannual variability in the atmospheric forcing and contaminates the eddy-
 562 mean flow decomposition (Figure 9). This is consistent with Aiki and Richards (2008)
 563 where they found the energy stored in the mean and eddy flow to change depending on
 564 the duration of the temporal averaging applied. While it is not our intention to claim
 565 whether defining the mean flow via a time mean is appropriate or not for realistic sim-
 566 ulations, our results imply that one should be mindful of what goes into defining the mean
 567 flow and consequently the eddies.

568 Lastly, ensemble modelling has shown us that a small perturbation such as eddies
 569 to the non-linear system can lead to very different states of the ocean and climate (e.g.
 570 Lorenz, 1963; Bessières et al., 2017; Maher et al., 2019; Jamet et al., 2019b; Uchida, Derem-
 571 ble, & Penduff, 2021; Fedele et al., 2021). In light of this, we argue that it is important
 572 to consider the full spatiotemporal variability of the ocean. The ensemble framework al-
 573 lows one to capture the space-time varying eddy-mean flow interaction and not just its
 574 climatological state.

575 **Appendix A Energetics under a non-linear equation of state**

576 In this Appendix, we derive the energetics in a similar manner to Aiki et al. (2016)
 577 but in a framework consistent with the ensemble formalism and a realistic EOS. The TWA

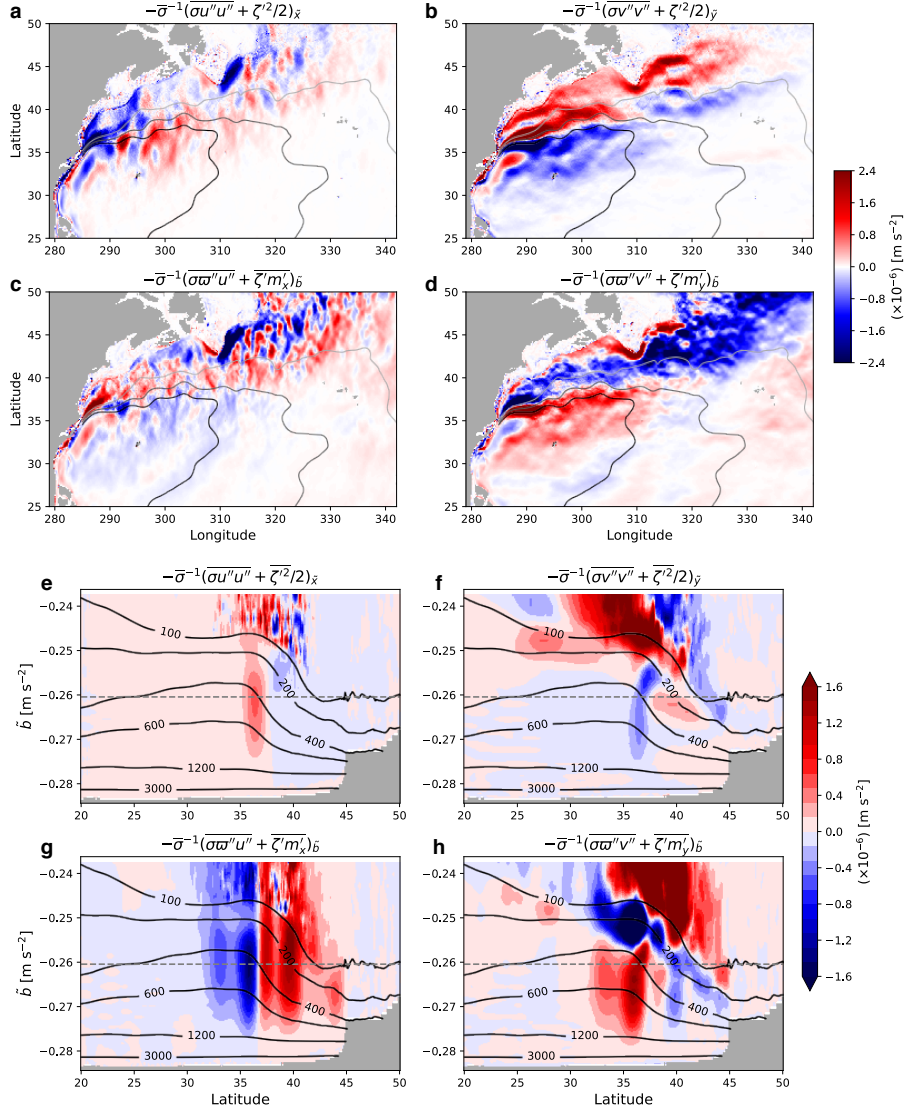


Figure 11. The annual mean of the convergence of eddy momentum flux and potential energy, and interfacial form stress for $\tilde{b} = -0.26$ **a-d**. The contours in grey shading east of 285°E indicate the 400, 300 and 200 m depth of the buoyancy surface. The annual and zonal mean transect between 290°E-305°E of the E-P flux convergence is shown in colored shading and ensemble-mean depth in black contours **e-h**. The iso-surface of buoyancy used through panels **a-d** is shown as the grey dashed line.

578 residual-mean horizontal momentum equation in geopotential coordinates neglecting dis-
 579 sipation is (Young, 2012; Ringler et al., 2017):

$$580 \quad \hat{\mathbf{u}}_t + \mathbf{v}^\# \cdot \nabla \hat{\mathbf{u}} + f \mathbf{k} \times \hat{\mathbf{u}} = -\nabla_h \phi^\# - \bar{\mathbf{e}} \cdot (\nabla \cdot \mathbf{E}), \quad (\text{A1})$$

581 where $\mathbf{v}^\# \stackrel{\text{def}}{=} \hat{u} \mathbf{i} + \hat{v} \mathbf{j} + w^\# \mathbf{k}$ and $\phi^\# \stackrel{\text{def}}{=} \bar{m}(\tilde{t}, \tilde{x}, \tilde{y}, b^\#(t, x, y, z)) + b^\# z$ are the residual-
 582 mean velocity and hydrostatic pressure anomaly. It is important to keep in mind that
 583 the “ z ” here is the ensemble averaged depth of an iso-surface of buoyancy, viz. $z = \bar{\zeta}(\tilde{t}, \tilde{x}, \tilde{y}, b^\#(t, x, y, z))$.
 584 The residual-mean kinetic energy (MKE; $K^\# = |\hat{\mathbf{u}}|^2/2$) budget becomes:

$$585 \quad \begin{aligned} K_t^\# + \mathbf{v}^\# \cdot \nabla K^\# &= -\hat{\mathbf{u}} \cdot \nabla_h \phi^\# - \hat{\mathbf{u}} \cdot [\bar{\mathbf{e}} \cdot (\nabla \cdot \mathbf{E})] \\ 586 &= -\hat{\mathbf{u}} \cdot \nabla_h \phi^\# - w^\# \phi_z^\# + w^\# \phi_z^\# - \hat{\mathbf{u}} \cdot [\bar{\mathbf{e}} \cdot (\nabla \cdot \mathbf{E})] \\ 587 &= -\mathbf{v}^\# \cdot \nabla \phi^\# + w^\# b^\# - \hat{\mathbf{u}} \cdot [\bar{\mathbf{e}} \cdot (\nabla \cdot \mathbf{E})]. \end{aligned} \quad (\text{A2})$$

589 We can now define the dynamic enthalpy for the mean state in a similar manner to McDougall
 590 (2003) and Young (2010):

$$591 \quad h^\# \stackrel{\text{def}}{=} \int_{\Phi_0}^{\Phi^\#} \frac{b^\#}{g} d\Phi^{\#'} = \int_z^0 b^\# dz', \quad (\text{A3})$$

592 where $\Phi^\# = \Phi_0 - gz$ is the dynamically non-active part of the hydrostatic pressure to
 593 be consistent with the Boussinesq approximation. Note that $h^\#$ is not a function of the
 594 TWA temperature and salinity $(\hat{\Theta}, \hat{S})$ due to non-linearities in the EOS, i.e. $\tilde{b}(\hat{\Theta}, \hat{S}, z) \neq$
 595 $\overline{\tilde{b}(\Theta, S, z)} = \tilde{b} = \tilde{b} = b^\#$. While there exist a temperature and salinity variable to
 596 evaluate the material derivative of $h^\#$ since an EOS exists for $b^\#$, it is unclear whether
 597 they can be analytically expressed for a non-linear EOS. We, therefore, express the ma-
 598 terial derivative of $h^\#$ as:

$$599 \quad \begin{aligned} \frac{D^\#}{Dt} h^\# &= h_z^\# \frac{D^\# z}{Dt} + \mathcal{H}^\# \\ 600 &= -w^\# b^\# + \mathcal{H}^\#, \end{aligned} \quad (\text{A4})$$

602 where $\mathcal{H}^\#$ carries the net sum of the diabatic and non-linear effects. Thus, the residual-
 603 mean total energy equation becomes:

$$604 \quad \frac{D^\#}{Dt} (K^\# + h^\#) = -\nabla \cdot \mathbf{v}^\# \phi^\# + \mathcal{H}^\# - \hat{\mathbf{u}} \cdot [\bar{\mathbf{e}} \cdot (\nabla \cdot \mathbf{E})], \quad (\text{A5})$$

605 where we have invoked $\nabla \cdot \mathbf{v}^\# = 0$.

606 On the other hand, the total KE budget remapped onto buoyancy coordinate is:

$$607 \quad \frac{DK}{Dt} = -\tilde{\nabla} \cdot \mathbf{v} \phi + w \tilde{b}, \quad (\text{A6})$$

608 where $\mathbf{v} \stackrel{\text{def}}{=} v^1 \mathbf{e}_1 + v^2 \mathbf{e}_2 + v^3 \mathbf{e}_3 = u \mathbf{e}_1 + v \mathbf{e}_2 + (\varpi + \frac{\zeta}{\sigma}) \mathbf{e}_3$ and $\tilde{\nabla} \cdot \mathbf{v} = \sigma^{-1} [(\sigma v^1)_{\bar{x}} + (\sigma v^2)_{\bar{y}} +$
 609 $(\sigma v^3)_{\bar{b}}]$ ($= 0$) is the three-dimensional divergence. Unlike the residual-mean dynamic
 610 enthalpy, the definition of the total dynamic enthalpy is straight forward (Young, 2010):

$$611 \quad h = \int_{\zeta}^0 \tilde{b}(\Theta, S, \zeta') d\zeta', \quad (\text{A7})$$

612 yielding:

$$613 \quad \frac{D}{Dt}(K + h) = -\tilde{\nabla} \cdot \mathbf{v} \phi + \mathcal{H}, \quad (\text{A8})$$

614 where $\mathcal{H} \stackrel{\text{def}}{=} h_{\Theta} \frac{D\Theta}{Dt} + h_S \frac{DS}{Dt}$. Terms due to non-linearity in the EOS do not emerge in
 615 the definition of \mathcal{H} as equation (A8) is not averaged. Ensemble averaging after thickness
 616 weighting equation (A8) gives:

$$617 \quad \overline{\sigma \frac{D}{Dt}(K + h)} = -\overline{\sigma \tilde{\nabla} \cdot \mathbf{v} \phi} + \overline{\sigma \mathcal{H}}$$

$$618 \quad = -\overline{\sigma \widehat{\tilde{\nabla} \cdot \mathbf{v} \phi}} + \overline{\sigma \widehat{\mathcal{H}}}, \quad (\text{A9})$$

620 The total KE can be expanded as:

$$621 \quad K = \frac{1}{2} |\hat{\mathbf{u}} + \mathbf{u}''|^2$$

$$622 \quad = \frac{|\hat{\mathbf{u}}|^2}{2} + \frac{|\mathbf{u}''|^2}{2} + \hat{u}u'' + \hat{v}v''$$

$$623 \quad \stackrel{\text{def}}{=} K^{\#} + \mathcal{K} + \hat{u}u'' + \hat{v}v'', \quad (\text{A10})$$

625 so plugging in equation (A10), and keeping in mind that $\overline{(\widehat{\cdot})} = \widehat{(\cdot)}$ and $\overline{\sigma(\cdot)''} = 0$, each
 626 term on the left-hand side (LHS) of equation (A9) can be written as:

$$627 \quad \overline{\sigma \frac{DK}{Dt}} = \overline{\sigma(K_{\bar{t}} + uK_{\bar{x}} + vK_{\bar{y}} + \varpi K_{\bar{b}})}$$

$$628 \quad = \overline{(\sigma K)_{\bar{t}}} + \overline{(\sigma u K)_{\bar{x}}} + \overline{(\sigma v K)_{\bar{y}}} + \overline{(\sigma \varpi K)_{\bar{b}}}$$

$$629 \quad = \overline{\sigma} \left[\frac{D^{\#}}{Dt}(K^{\#} + \widehat{\mathcal{K}}) + \tilde{\nabla} \cdot (\mathbf{J}^K + \hat{u} \mathbf{J}^u + \hat{v} \mathbf{J}^v) \right], \quad (\text{A11})$$

631 where $\widehat{\mathcal{K}}$ is the eddy kinetic energy (EKE), and $\mathbf{J}^K \stackrel{\text{def}}{=} \widehat{u'' \mathcal{K}} \mathbf{e}_1 + \widehat{v'' \mathcal{K}} \mathbf{e}_2 + \widehat{\varpi'' \mathcal{K}} \mathbf{e}_3$,
 632 $\mathbf{J}^u \stackrel{\text{def}}{=} \widehat{u''^2} \mathbf{e}_1 + \widehat{v'' u''} \mathbf{e}_2 + \widehat{\varpi'' u''} \mathbf{e}_3$, $\mathbf{J}^v \stackrel{\text{def}}{=} \widehat{u'' v''} \mathbf{e}_1 + \widehat{v''^2} \mathbf{e}_2 + \widehat{\varpi'' v''} \mathbf{e}_3$ are the eddy fluxes
 633 of kinetic energy, eddy zonal and meridional velocities respectively, and

$$634 \quad \overline{\sigma \frac{Dh}{Dt}} = \overline{\sigma(h_{\bar{t}} + uh_{\bar{x}} + vh_{\bar{y}} + \varpi h_{\bar{b}})}$$

$$635 \quad = \overline{(\sigma h)_{\bar{t}}} + \overline{(\sigma u h)_{\bar{x}}} + \overline{(\sigma v h)_{\bar{y}}} + \overline{(\sigma \varpi h)_{\bar{b}}}$$

$$636 \quad = \overline{(\sigma \hat{h})_{\bar{t}}} + \overline{[\sigma(\hat{u} \hat{h} + \widehat{u'' h''})]_{\bar{x}}} + \overline{[\sigma(\hat{v} \hat{h} + \widehat{v'' h''})]_{\bar{y}}} + \overline{[\sigma(\hat{\varpi} \hat{h} + \widehat{\varpi'' h''})]_{\bar{b}}}$$

$$637 \quad = \overline{\sigma} \left(\frac{D^{\#}}{Dt} \hat{h} + \tilde{\nabla} \cdot \mathbf{J}^h \right), \quad (\text{A12})$$

639 where $\mathbf{J}^h \stackrel{\text{def}}{=} \widehat{u''h''}\mathbf{e}_1 + \widehat{v''h''}\mathbf{e}_2 + \widehat{\varpi''h''}\mathbf{e}_3$ is the eddy flux of fluctuations in dynamic
 640 enthalpy, and we have used the relation $\overline{\sigma\phi\theta} = \overline{\sigma(\hat{\phi}\hat{\theta} + \hat{\phi}''\hat{\theta}'')}$ (equation (72) in Young,
 641 2012). Hence, combining equations (A11) and (A12), equation (A9) becomes:

$$642 \quad \frac{D^\#}{Dt}(K^\# + \widehat{\mathcal{H}} + \hat{h}) = -\tilde{\nabla} \cdot (\mathbf{J}^K + \mathbf{J}^h + \hat{u}\mathbf{J}^u + \hat{v}\mathbf{J}^v) - \tilde{\nabla} \cdot \widehat{\mathbf{v}\phi} + \widehat{\mathcal{H}}. \quad (\text{A13})$$

643 Subtracting equation (A5) from (A13) yields the eddy energy budget:

$$644 \quad \frac{D^\#}{Dt}(\widehat{\mathcal{H}} + \hat{h} - h^\#) = -(\tilde{\nabla} \cdot \widehat{\mathbf{v}\phi} - \nabla \cdot \mathbf{v}^\#\phi^\#) - \tilde{\nabla} \cdot (\mathbf{J}^K + \mathbf{J}^h + \hat{u}\mathbf{J}^u + \hat{v}\mathbf{J}^v) \\ 645 \quad \quad \quad + \widehat{\mathcal{H}} - \mathcal{H}^\# + \hat{\mathbf{u}} \cdot [\bar{\mathbf{e}} \cdot (\nabla \cdot \mathbf{E})]. \quad (\text{A14})$$

647 Equations (A5) and (A14) are the relations derived by Aoki (2014) but for a non-linear
 648 EOS and non-zero dia-surface velocity where the residual-mean flow and eddies exchange
 649 energy via the E-P flux divergence and residual vertical buoyancy flux due to non-linearities
 650 in the EOS. It is perhaps interesting to note that h'' is not the eddy potential energy (EPE;
 651 $\widehat{\mathcal{H}} \stackrel{\text{def}}{=} \hat{h} - h^\#$ in equation (A14)) and they are related to one another as $h'' = h -$
 652 $(h^\# + \widehat{\mathcal{H}})$.

653 For a linear EOS, the EPE can be rewritten as:

$$654 \quad \widehat{\mathcal{H}} = -b^\#(\hat{\zeta} - \bar{\zeta}) = -b^\# \frac{\overline{\sigma'\zeta'}}{\bar{\sigma}}, \quad (\text{A15})$$

656 by taking advantage of $\hat{h} = -\tilde{b}\hat{\zeta}$, $h^\# = -b^\#\bar{\zeta}$ and $\tilde{b} = \tilde{b} = b^\#(t, x, y, \bar{\zeta}(\tilde{t}, \tilde{x}, \tilde{y}, \tilde{b}))$.

657 Equation (A15) provides the physical intuition of EPE being defined as the difference
 658 between potential energy at the TWA depth ($\hat{\zeta}$) and ensemble-mean depth ($\bar{\zeta}$). In a sim-
 659 ilar manner, we can also derive:

$$660 \quad h'' = -\tilde{b}(\zeta - \hat{\zeta}) = -\tilde{b}\zeta'', \quad (\text{A16})$$

661 and hence, $\overline{h''} = -\widehat{\mathcal{H}}$. Assuming the background buoyancy frequency can be defined
 662 as the inverse of ensemble-mean thickness (viz. $\bar{\sigma}^{-1} \sim N^2$) leads to further manipu-
 663 lation of EPE:

$$664 \quad \widehat{\mathcal{H}} \sim -b^\#N^2\overline{\zeta'_b\zeta'} = -b^\#N^2\left(\frac{\overline{\zeta'^2}}{2}\right)_{\tilde{b}} \\ 665 \quad \quad \quad = -N^2\left[\left(b^\#\frac{\overline{\zeta'^2}}{2}\right)_{\tilde{b}} - \frac{\overline{\zeta'^2}}{2}\right], \quad (\text{A17})$$

667 where the last term in equation (A17) further reduces to the available potential energy
 668 under quasi-geostrophic approximation ($b' \sim N^2\zeta'$). The first-term on the RHS of equa-
 669 tion (A17) vanishes upon volume integration pending on boundary conditions (i.e. rigid
 670 lid and a flat bottom).

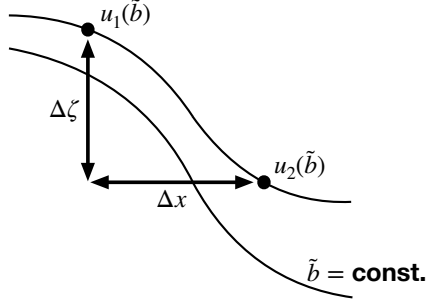


Figure B1. Schematic of discretized gradients.

Appendix B Kinematics of discretization

As in Figure B1, imagine u_1 and u_2 are on the same buoyancy contour. The relation between the two is:

$$u_2 \approx u_1 + u_x \Delta x + u_\zeta \Delta \zeta. \quad (\text{B1})$$

Now,

$$\begin{aligned} u_{\bar{x}} &\stackrel{\text{def}}{=} u_x + \frac{\Delta \zeta}{\Delta x} \sigma^{-1} u_{\tilde{b}} \\ &= u_x + \frac{\Delta \zeta}{\Delta x} u_\zeta \\ &= \frac{u_2 - u_1}{\Delta x} \quad (\because \text{equation (B1)}), \end{aligned} \quad (\text{B2})$$

so once all of the variables are remapped onto the buoyancy coordinate from geopotential, the discretized horizontal gradients can be taken along the original Cartesian grid. The gradients on the model outputs were taken using the `xgcm` Python package (Abernathey et al., 2021; Busecke & Abernathey, 2020). In order to minimize the computational cost, we took the ensemble mean first whenever possible, e.g. $\bar{\sigma} = \overline{\partial_{\tilde{b}} \zeta} = \partial_{\tilde{b}} \bar{\zeta}$, $\tilde{\nabla}_h \bar{\sigma} = \partial_{\tilde{b}} \tilde{\nabla}_h \bar{\zeta}$ etc. The gradient operators commuting with the ensemble mean is also the case for the perturbations, i.e.

$$\tilde{\nabla}_h (\bar{m} + m') = \tilde{\nabla}_h m = \overline{\tilde{\nabla}_h m} + (\tilde{\nabla}_h m)'. \quad (\text{B3})$$

Hence, $\tilde{\nabla}_h m' = (\tilde{\nabla}_h m)'$ (cf. Maddison & Marshall, 2013, Section 2.3 in their paper).

Acknowledgments

This research was funded by the French ‘Make Our Planet Great Again’ (MOPGA) initiative managed by the Agence Nationale de la Recherche under the Programme d’Investissement d’Avenir, with the reference ANR-18-MPGA-0002. High-performance computing resources on Cheyenne (doi:10.5065/D6RX99HX) used for running the ensembles were provided

694 by NCAR’s Computational and Information Systems Laboratory, sponsored by the Na-
 695 tional Science Foundation, under the university large allocation UFSU0011. This study
 696 is a contribution to the ‘Assessing the Role of forced and internal Variability for the Ocean
 697 and climate Response in a changing climate’ (ARVOR) project supported by the French
 698 ‘Les Enveloppes Fluides et l’Environnement’ (LEFE) program. Dewar acknowledges sup-
 699 port from the NSF grants OCE-1829856 and OCE-1941963. Balwada acknowledges sup-
 700 port from the NSF grant OCE-1756882. We thank the editor Stephen Griffies, along with
 701 Laure Zanna and four other anonymous reviewers for their constructive and careful re-
 702 views, which lead to significant improvements in the manuscript. We would like to thank
 703 Geoffrey Stanley and Trevor McDougall for insightful discussions regarding the buoy-
 704 ancy coordinate for a realistic EOS. The simulation outputs are available on the Florida
 705 State University cluster (<http://ocean.fsu.edu/~qjemet/share/data/Uchida2021/>).
 706 We also acknowledge Edward Peirce and Kelly Hirai for maintaining the cluster upon
 707 which the data analyses were conducted. Python scripts used for the off-line diagnosis
 708 are available on Github ([doi:10.5281/zenodo.5823419](https://doi.org/10.5281/zenodo.5823419)). Uchida acknowledges the `xarray`
 709 (Hoyer et al., 2021) and `dask` (Rocklin et al., 2021) Python package developers for par-
 710 allelizing the analysis.

711 References

- 712 Abernathey, R. P. (2020). `fastjmd95`: *Numba implementation of Jackett & Mc-*
 713 *Dougall (1995) ocean equation of state*. Retrieved from [https://github.com/](https://github.com/xgcm/fastjmd95)
 714 [xgcm/fastjmd95](https://github.com/xgcm/fastjmd95)
- 715 Abernathey, R. P., Busecke, J., Smith, T., Banihirwe, A., Fernandes, F., Bourbeau,
 716 J., et al. (2021). `xgcm`: *General circulation model postprocessing with xar-*
 717 *ray*. Retrieved from <https://xgcm.readthedocs.io/en/latest/> doi:
 718 10.5281/zenodo.3634752
- 719 Aiki, H., & Richards, K. J. (2008). Energetics of the global ocean: the role of layer-
 720 thickness form drag. *Journal of Physical Oceanography*, 38(9), 1845–1869. doi:
 721 10.1175/2008JPO3820.1
- 722 Aiki, H., Zhai, X., & Greatbatch, R. J. (2016). *Energetics of the global ocean: The*
 723 *role of mesoscale eddies*. World Scientific. doi: 10.1142/9789814696623_0004
- 724 Ajayi, A., Le Sommer, J., Chassignet, E., Molines, J.-M., Xu, X., Albert, A., &
 725 Cosme, E. (2020). Spatial and temporal variability of the north atlantic eddy
 726 field from two kilometeric-resolution ocean models. *Journal of Geophysical*

- 727 *Research: Oceans*. doi: 10.1029/2019JC015827
- 728 Aluie, H., Hecht, M., & Vallis, G. K. (2018). Mapping the energy cascade in the
 729 north atlantic ocean: The coarse-graining approach. *Journal of Physical*
 730 *Oceanography*, *48*(2), 225–244. doi: 10.1175/JPO-D-17-0100.1
- 731 Andrews, D. G. (1983). A finite-amplitude Eliassen-Palm theorem in isentropic co-
 732 ordinates. *Journal of Atmospheric Sciences*, *40*(8), 1877–1883. doi: 10.1175/
 733 1520-0469(1983)040<1877:AFAEPT>2.0.CO;2
- 734 Aoki, K. (2014). A constraint on the thickness-weighted average equation of motion
 735 deduced from energetics. *Journal of Marine Research*, *72*(5), 355–382. doi: 10
 736 .1357/002224014815469886
- 737 Aoki, K., Kubokawa, A., Furue, R., & Sasaki, H. (2016). Influence of eddy momen-
 738 tum fluxes on the mean flow of the Kuroshio extension in a 1/10 ocean general
 739 circulation model. *Journal of Physical Oceanography*, *46*(9), 2769–2784. doi:
 740 10.1175/JPO-D-16-0021.1
- 741 Arbic, B. K., Polzin, K. L., Scott, R. B., Richman, J. G., & Shriver, J. F. (2013).
 742 On eddy viscosity, energy cascades, and the horizontal resolution of gridded
 743 satellite altimeter products. *Journal of Physical Oceanography*, *43*(2), 283–300.
 744 doi: 10.1175/JPO-D-11-0240.1
- 745 Bachman, S. D. (2019). The GM+E closure: A framework for coupling backscatter
 746 with the Gent and McWilliams parameterization. *Ocean Modelling*, *136*, 85–
 747 106. doi: 10.1016/j.ocemod.2019.02.006
- 748 Bachman, S. D., Anstey, J. A., & Zanna, L. (2018). The relationship between a
 749 deformation-based eddy parameterization and the LANS- α turbulence model.
 750 *Ocean Modelling*, *126*, 56–62. doi: 10.1016/j.ocemod.2018.04.007
- 751 Bachman, S. D., Fox-Kemper, B., & Bryan, F. O. (2015). A tracer-based inver-
 752 sion method for diagnosing eddy-induced diffusivity and advection. *Ocean*
 753 *Modelling*, *86*, 1–14. doi: 10.1016/j.ocemod.2014.11.006
- 754 Balwada, D., Smith, S. K., & Abernathey, R. P. (2018). Submesoscale verti-
 755 cal velocities enhance tracer subduction in an idealized Antarctic Circum-
 756 polar Current. *Geophysical Research Letters*, *45*(18), 9790–9802. doi:
 757 10.1029/2018GL079244
- 758 Berloff, P. (2018). Dynamically consistent parameterization of mesoscale eddies.
 759 Part III: Deterministic approach. *Ocean Modelling*, *127*, 1–15. doi: 10.1016/

760 j.ocemod.2018.04.009

- 761 Bessières, L., Leroux, S., Brankart, J.-M., Molines, J.-M., Moine, M.-P., Bouttier,
 762 P.-A., ... Sérazin, G. (2017). Development of a probabilistic ocean modelling
 763 system based on NEMO 3.5: application at eddying resolution. *Geoscientific*
 764 *Model Development*, 10(3), 1091–1106. doi: 10.5194/gmd-10-1091-2017
- 765 Bire, S., & Wolfe, C. L. (2018). The role of eddies in buoyancy-driven eastern
 766 boundary currents. *Journal of Physical Oceanography*, 48(12), 2829–2850. doi:
 767 10.1175/JPO-D-18-0040.1
- 768 Boccaletti, G., Ferrari, R., & Fox-Kemper, B. (2007). Mixed layer instabilities and
 769 restratification. *Journal of Physical Oceanography*, 37(9), 2228–2250.
- 770 Bühler, O. (2014). *Waves and mean flows*. Cambridge University Press. doi: 10
 771 .1017/CBO9781107478701
- 772 Busecke, J., & Abernathey, R. P. (2020). CMIP6 without the interpolation: Grid-
 773 native analysis with pangeo in the cloud. In *Earthcube annual meeting*. Re-
 774 trieved from https://github.com/earthcube2020/ec20_busecke_etal
- 775 Capet, X., McWilliams, J. C., Molemaker, M. J., & Shchepetkin, A. F. (2008a).
 776 Mesoscale to submesoscale transition in the California current system. Part I:
 777 Flow structure, eddy flux, and observational tests. *Journal of physical oceanog-*
 778 *raphy*, 38(1), 29–43. doi: 10.1175/2007JPO3671.1
- 779 Capet, X., McWilliams, J. C., Molemaker, M. J., & Shchepetkin, A. F. (2008b).
 780 Mesoscale to submesoscale transition in the California Current system. Part
 781 III: Energy balance and flux. *Journal of Physical Oceanography*, 38(10), 2256–
 782 2269. doi: <https://doi.org/10.1175/2008JPO3810.1>
- 783 Cessi, P., & Wolfe, C. L. (2013). Adiabatic eastern boundary currents. *Journal of*
 784 *Physical Oceanography*, 43(6), 1127–1149. doi: 10.1175/JPO-D-12-0211.1
- 785 Chan, C. J., Plumb, R. A., & Cerovecki, I. (2007). Annular modes in a multiple
 786 migrating zonal jet regime. *Journal of the atmospheric sciences*, 64(11), 4053–
 787 4068. doi: 10.1175/2007JAS2156.1
- 788 Chassignet, E. P., & Xu, X. (2017). Impact of horizontal resolution ($1/12^\circ$ to
 789 $1/50^\circ$) on Gulf Stream separation, penetration, and variability. *Journal of*
 790 *Physical Oceanography*, 47(8), 1999–2021. doi: 10.1175/JPO-D-17-0031.1
- 791 Chassignet, E. P., & Xu, X. (2021). On the importance of high-resolution in large-
 792 scale ocean models. *Advances in Atmospheric Sciences*, 1–14. doi: 10.1007/

793 s00376-021-0385-7

794 Chemke, R., & Kaspi, Y. (2015). Poleward migration of eddy-driven jets.
795 *Journal of Advances in Modeling Earth Systems*, 7(3), 1457–1471. doi:
796 10.1002/2015MS000481

797 Cronin, M. (1996). Eddy-mean flow interaction in the gulf stream at 68 W. Part
798 II: Eddy forcing on the time-mean flow. *Journal of Physical Oceanography*,
799 26(10), 2132–2151. doi: 10.1175/1520-0485(1996)026<2132:EMFIIT>2.0.CO;2

800 de Boyer Montégut, C., Madec, G., Fischer, A. S., Lazar, A., & Iudicone, D. (2004).
801 Mixed layer depth over the global ocean: An examination of profile data and a
802 profile-based climatology. *Journal of Geophysical Research: Oceans*, 109(C12).
803 doi: 10.1029/2004JC002378

804 Deremble, B., Wienders, N., & Dewar, W. (2013). CheapAML: A simple, at-
805 mospheric boundary layer model for use in ocean-only model calculations.
806 *Monthly weather review*, 141(2), 809–821. doi: 10.1175/MWR-D-11-00254.1

807 de Szoeké, R. A., & Bennett, A. F. (1993). Microstructure fluxes across density sur-
808 faces. *Journal of Physical Oceanography*, 23(10), 2254–2264. doi: 10.1175/1520
809 -0485(1993)023<2254:MFADS>2.0.CO;2

810 de Szoeké, R. A., & Springer, S. R. (2009). The materiality and neutrality of neu-
811 tral density and orthobaric density. *Journal of Physical Oceanography*, 39(8),
812 1779–1799. doi: 10.1175/2009JPO4042.1

813 Fairall, C. W., Bradley, E. F., Hare, J. E., Grachev, A. A., & Edson, J. B.
814 (2003). Bulk parameterization of air–sea fluxes: Updates and verifica-
815 tion for the COARE algorithm. *Journal of climate*, 16(4), 571–591. doi:
816 10.1175/1520-0442(2003)016<0571:BPOASF>2.0.CO;2

817 Fedele, G., Penduff, T., Pierini, S., Alvarez-Castro, M. C., Bellucci, A., & Masina, S.
818 (2021). Interannual to decadal variability of the Kuroshio extension: analyzing
819 an ensemble of global hindcasts from a dynamical system viewpoint. *Climate*
820 *Dynamics*, 1–18. doi: 10.1007/s00382-021-05751-7

821 Fofonoff, N. (1981). *The Gulf Stream system. Evolution of physical oceanography*.
822 MIT Press. Retrieved from [https://ocw.mit.edu/ans7870/textbooks/
823 Wunsch/Edited/Chapter4.pdf](https://ocw.mit.edu/ans7870/textbooks/Wunsch/Edited/Chapter4.pdf)

824 Gallimore, R. G., & Johnson, D. R. (1981). The forcing of the meridional circulation
825 of the isentropic zonally averaged circumpolar vortex. *Journal of Atmospheric*

- 826 *Sciences*, 38(3), 583–599. doi: 10.1175/1520-0469(1981)038<0583:TFOTMC>2.0
 827 .CO;2
- 828 Greatbatch, R. J. (1998). Exploring the relationship between eddy-induced
 829 transport velocity, vertical momentum transfer, and the isopycnal flux of
 830 potential vorticity. *Journal of Physical Oceanography*, 28(3), 422–432. doi:
 831 10.1175/1520-0485(1998)028<0422:ETRBEI>2.0.CO;2
- 832 Griffies, S. M., Winton, M., Anderson, W. G., Benson, R., Delworth, T. L., Dufour,
 833 C. O., ... others (2015). Impacts on ocean heat from transient mesoscale
 834 eddies in a hierarchy of climate models. *Journal of Climate*, 28(3), 952–977.
 835 doi: 10.1175/JCLI-D-14-00353.1
- 836 Grooms, I., Julien, K., & Fox-Kemper, B. (2011). On the interactions between plan-
 837 etary geostrophy and mesoscale eddies. *Dynamics of atmospheres and oceans*,
 838 51(3), 109–136. doi: 10.1016/j.dynatmoce.2011.02.002
- 839 Guillaumin, A. P., & Zanna, L. (2021). Stochastic-deep learning parameterization
 840 of ocean momentum forcing. *Journal of Advances in Modeling Earth Systems*,
 841 13(9), e2021MS002534. doi: 10.1029/2021MS002534
- 842 Hoyer, S., Abernathy, R. P., Hamman, J., Bovy, B., Maussion, F., Fujii, K.,
 843 ... others (2021). *xarray: N-d labeled arrays and datasets*. Retrieved
 844 from <http://xarray.pydata.org/en/stable/index.html> doi: 10.5281/
 845 zenodo.598201
- 846 Jackett, D. R., & McDougall, T. J. (1995). Minimal adjustment of hydrographic pro-
 847 files to achieve static stability. *Journal of Atmospheric and Oceanic Technol-
 848 ogy*, 12(2), 381–389. doi: 10.1175/1520-0426(1995)012<0381:MAOHPT>2.0.CO;
 849 2
- 850 Jackett, D. R., & McDougall, T. J. (1997). A neutral density variable for the world’s
 851 oceans. *Journal of Physical Oceanography*, 27(2), 237–263. doi: 10.1175/1520-
 852 -0485(1997)027<0237:ANDVFT>2.0.CO;2
- 853 Jamet, Q., Deremble, B., Wienders, N., Uchida, T., & Dewar, W. K. (2021). On
 854 wind-driven energetics of subtropical gyres. *Journal of Advances in Modelling
 855 Earth Systems*, e2020MS002329. doi: 10.1029/2020MS002329
- 856 Jamet, Q., Dewar, W. K., Wienders, N., & Deremble, B. (2019a). Fast warming
 857 of the surface ocean under a climatological scenario. *Geophysical Research Let-
 858 ters*, 46(7), 3871–3879. doi: 10.1029/2019GL082336

- 859 Jamet, Q., Dewar, W. K., Wienders, N., & Deremble, B. (2019b). Spatiotempo-
 860 ral patterns of chaos in the Atlantic Overturning Circulation. *Geophysical Re-*
 861 *search Letters*, *46*(13), 7509–7517. doi: 10.1029/2019GL082552
- 862 Jamet, Q., Dewar, W. K., Wienders, N., Deremble, B., Close, S., & Penduff, T.
 863 (2020). Locally and remotely forced subtropical AMOC variability: A matter
 864 of time scales. *Journal of Climate*. doi: 10.1175/JCLI-D-19-0844.1
- 865 Jansen, M. F., Adcroft, A., Khani, S., & Kong, H. (2019). Toward an energetically
 866 consistent, resolution aware parameterization of ocean mesoscale eddies. *Jour-*
 867 *nal of Advances in Modeling Earth Systems*, *11*(8), 2844–2860. doi: 10.1029/
 868 2019MS001750
- 869 Jones, S. C., Busecke, J., Uchida, T., & Abernathy, R. P. (2020). Vertical re-
 870 gridding and remapping of CMIP6 ocean data in the cloud. In *Earthcube*
 871 *annual meeting*. Retrieved from [https://github.com/earthcube2020/](https://github.com/earthcube2020/ec20-jones_etal)
 872 [ec20-jones_etal](https://github.com/earthcube2020/ec20-jones_etal)
- 873 Juricke, S., Danilov, S., Koldunov, N., Oliver, M., & Sidorenko, D. (2020). Ocean
 874 kinetic energy backscatter parametrization on unstructured grids: Impact on
 875 global eddy-permitting simulations. *Journal of Advances in Modeling Earth*
 876 *Systems*, *12*(1). doi: 10.1029/2019MS001855
- 877 Kitsios, V., Frederiksen, J. S., & Zidikheri, M. J. (2013). Scaling laws for pa-
 878 rameterisations of subgrid eddy–eddy interactions in simulations of oceanic
 879 circulations. *Ocean Modelling*, *68*, 88–105. doi: 10.1016/j.ocemod.2013.05.001
- 880 Kjellsson, J., & Zanna, L. (2017). The impact of horizontal resolution on energy
 881 transfers in global ocean models. *Fluids*, *2*(3), 45. doi: 10.3390/fluids2030045
- 882 Klocker, A., McDougall, T. J., & Jackett, D. R. (2009). A new method for forming
 883 approximately neutral surfaces. *Ocean Science*, *5*(2), 155–172. doi: 10.5194/os
 884 -5-155-2009
- 885 Lang, Y., Stanley, G. J., McDougall, T. J., & Barker, P. M. (2020). A pressure-
 886 invariant neutral density variable for the World’s Oceans. *Journal of Physical*
 887 *Oceanography*, 1–58. doi: 10.1175/JPO-D-19-0321.1
- 888 Leroux, S., Penduff, T., Bessières, L., Molines, J.-M., Brankart, J.-M., Sérazin, G.,
 889 ... Terray, L. (2018). Intrinsic and atmospherically forced variability of the
 890 AMOC: Insights from a large-ensemble ocean hindcast. *Journal of Climate*,
 891 *31*(3), 1183–1203. doi: 10.1175/JCLI-D-17-0168.1

- 892 Lévy, M., Klein, P., Tréguier, A.-M., Iovino, D., Madec, G., Masson, S., & Taka-
 893 hashi, K. (2010). Modifications of gyre circulation by sub-mesoscale physics.
 894 *Ocean Modelling*, *34*(1-2), 1–15. doi: 10.1016/j.ocemod.2010.04.001
- 895 Lévy, M., Resplandy, L., Klein, P., Capet, X., Iovino, D., & Éthé, C. (2012).
 896 Grid degradation of submesoscale resolving ocean models: Benefits for of-
 897 fine passive tracer transport. *Ocean Modelling*, *48*, 1–9. doi: 10.1016/
 898 j.ocemod.2012.02.004
- 899 Lorenz, E. N. (1963). Deterministic nonperiodic flow. *Journal of atmospheric sci-*
 900 *ences*, *20*(2), 130–141. doi: 10.1175/1520-0469(1963)020<0130:DNF>2.0.CO;2
- 901 Maddison, J. R., & Marshall, D. P. (2013). The Eliassen–Palm flux tensor. *Journal*
 902 *of Fluid Mechanics*, *729*, 69–102. doi: 10.1017/jfm.2013.259
- 903 Maher, N., Milinski, S., Suarez-Gutierrez, L., Botzet, M., Dobrynin, M., Kornblueh,
 904 L., ... others (2019). The Max Planck Institute grand ensemble: Enabling
 905 the exploration of climate system variability. *Journal of Advances in Modeling*
 906 *Earth Systems*, *11*(7), 2050–2069. doi: 10.1029/2019MS001639
- 907 Marshall, D. P., Maddison, J. R., & Berloff, P. S. (2012). A framework for pa-
 908 rameterizing eddy potential vorticity fluxes. *Journal of Physical Oceanography*,
 909 *42*(4), 539–557. doi: 10.1175/JPO-D-11-048.1
- 910 Marshall, J., Hill, C., Perelman, L., & Adcroft, A. (1997). Hydrostatic, quasi-
 911 hydrostatic, and nonhydrostatic ocean modeling. *Journal of Geophysical*
 912 *Research: Oceans*, *102*(C3), 5733–5752. doi: 10.1029/96JC02776
- 913 McDougall, T. J. (2003). Potential enthalpy: A conservative oceanic variable for
 914 evaluating heat content and heat fluxes. *Journal of Physical Oceanography*,
 915 *33*(5), 945–963. doi: 10.1175/1520-0485(2003)033<0945:PEACOV>2.0.CO;2
- 916 McDougall, T. J., & Jackett, D. R. (2005). An assessment of orthobaric density in
 917 the global ocean. *Journal of Physical Oceanography*, *35*(11), 2054–2075. doi:
 918 10.1175/JPO2796.1
- 919 McDougall, T. J., & McIntosh, P. C. (2001). The temporal-residual-mean ve-
 920 locity. Part II: Isopycnal interpretation and the tracer and momentum
 921 equations. *Journal of Physical Oceanography*, *31*(5), 1222–1246. doi:
 922 10.1175/1520-0485(2001)031<1222:TTRMVP>2.0.CO;2
- 923 Molines, J.-M., Barnier, B., Penduff, T., Treguier, A., & Le Sommer, J. (2014).
 924 ORCA12. L46 climatological and interannual simulations forced with DFS4.

- 925 4: GJM02 and MJM88. drakkar group experiment rep. tech. rep. In *Gdri-*
 926 *drakkar-2014-03-19* (p. 50). Retrieved from [http://www.drakkar-ocean.eu/](http://www.drakkar-ocean.eu/publications/reports/orca12referenceexperiments2014)
 927 [publications/reports/orca12referenceexperiments2014](http://www.drakkar-ocean.eu/publications/reports/orca12referenceexperiments2014)
- 928 Montgomery, R. B. (1937). A suggested method for representing gradient flow in
 929 isentropic surfaces. *Bulletin of the American Meteorological Society*, 18(6-7),
 930 210–212. doi: 10.1175/1520-0477-18.6-7.210
- 931 Olbers, D., Willebrand, J., & Eden, C. (2012). *Ocean dynamics*. Springer Science &
 932 Business Media.
- 933 Perezhogin, P. (2019). Deterministic and stochastic parameterizations of kinetic
 934 energy backscatter in the NEMO ocean model in double-gyre configuration. In
 935 *Top conference series: Earth and environmental science* (Vol. 386, p. 012025).
 936 doi: 10.1088/1755-1315/386/1/012025
- 937 Renault, L., Molemaker, M. J., Gula, J., Masson, S., & McWilliams, J. C. (2016).
 938 Control and stabilization of the gulf stream by oceanic current interaction with
 939 the atmosphere. *Journal of Physical Oceanography*, 46(11), 3439–3453. doi:
 940 10.1175/JPO-D-16-0115.1
- 941 Ringler, T., Saenz, J. A., Wolfram, P. J., & Van Roekel, L. (2017). A thickness-
 942 weighted average perspective of force balance in an idealized circumpo-
 943 lar current. *Journal of Physical Oceanography*, 47(2), 285–302. doi:
 944 10.1175/JPO-D-16-0096.1
- 945 Rocklin, M., Crist-Harif, J., Bourbeau, J., Augspurger, T., Durant, M., Signell, J.,
 946 ... others (2021). *dask: Parallel computing with task scheduling*. Retrieved
 947 from <https://dask.org/>
- 948 Sasaki, H., Klein, P., Qiu, B., & Sasai, Y. (2014). Impact of oceanic-scale inter-
 949 actions on the seasonal modulation of ocean dynamics by the atmosphere. *Na-*
 950 *nature communications*, 5(1), 1–8. doi: 10.1038/ncomms6636
- 951 Schubert, R., Jonathan, G., Greatbatch, R. J., Baschek, B., & Biastoch, A. (2020).
 952 The submesoscale kinetic energy cascade: Mesoscale absorption of subme-
 953 soscale mixed-layer eddies and frontal downscale fluxes. *Journal of Physical*
 954 *Oceanography*. doi: 10.1175/JPO-D-19-0311.1
- 955 Sérazin, G., Jaymond, A., Leroux, S., Penduff, T., Bessières, L., Llovel, W., ...
 956 Terray, L. (2017). A global probabilistic study of the ocean heat content low-
 957 frequency variability: Atmospheric forcing versus oceanic chaos. *Geophysical*

- 958 *Research Letters*, 44(11), 5580–5589. doi: 10.1002/2017GL073026
- 959 Stammer, D. (1997). Global characteristics of ocean variability estimated from
 960 regional TOPEX/POSEIDON altimeter measurements. *Journal of Physical*
 961 *Oceanography*, 27(8), 1743–1769. doi: 10.1175/1520-0485(1997)027<1743:
 962 GCOOVE>2.0.CO;2
- 963 Stanley, G. J. (2018). *Tales from topological oceans* (Doctoral dissertation, Uni-
 964 versity of Oxford). Retrieved from [https://ora.ox.ac.uk/objects/uuid:](https://ora.ox.ac.uk/objects/uuid:414355e6-ba26-4004-bc71-51e4fa5fb1bb)
 965 [414355e6-ba26-4004-bc71-51e4fa5fb1bb](https://ora.ox.ac.uk/objects/uuid:414355e6-ba26-4004-bc71-51e4fa5fb1bb)
- 966 Stanley, G. J. (2019). Neutral surface topology. *Ocean Modelling*, 138, 88–106. doi:
 967 10.1016/j.ocemod.2019.01.008
- 968 Su, Z., Wang, J., Klein, P., Thompson, A. F., & Menemenlis, D. (2018). Ocean sub-
 969 mesoscales as a key component of the global heat budget. *Nature communica-*
 970 *tions*, 9(1), 775. doi: 10.1038/s41467-018-02983-w
- 971 Tailleux, R. (2016). Generalized patched potential density and thermodynamic
 972 neutral density: Two new physically based quasi-neutral density variables
 973 for ocean water masses analyses and circulation studies. *Journal of Physical*
 974 *Oceanography*, 46(12), 3571–3584. doi: 10.1175/JPO-D-16-0072.1
- 975 Uchida, T., Abernathy, R. P., & Smith, S. K. (2017). Seasonality of eddy kinetic
 976 energy in an eddy permitting global climate model. *Ocean Modelling*, 118, 41–
 977 58. doi: 10.1016/j.ocemod.2017.08.006
- 978 Uchida, T., Balwada, D., Abernathy, R. P., McKinley, G. A., Smith, S. K., & Lévy,
 979 M. (2019). The contribution of submesoscale over mesoscale eddy iron trans-
 980 port in the open Southern Ocean. *Journal of Advances in Modeling Earth*
 981 *Systems*, 11, 3934–3958. doi: 10.1029/2019MS001805
- 982 Uchida, T., Deremble, B., Dewar, W. K., & Penduff, T. (2021). Diagnosing the
 983 Eliassen-Palm flux from a quasi-geostrophic double gyre ensemble. In *Earth-*
 984 *cube annual meeting*. Retrieved from [https://earthcube2021.github.io/](https://earthcube2021.github.io/ec21_book/notebooks/ec21_uchida_et_al/notebooks/TU.05_Diagnosing-the-Eliassen-Palm-flux-from-a-quasi-geostrophic-double-gyre-ensemble.html)
 985 [ec21_book/notebooks/ec21_uchida_et_al/notebooks/TU.05_Diagnosing-the](https://earthcube2021.github.io/ec21_book/notebooks/ec21_uchida_et_al/notebooks/TU.05_Diagnosing-the-Eliassen-Palm-flux-from-a-quasi-geostrophic-double-gyre-ensemble.html)
 986 [-Eliassen-Palm-flux-from-a-quasi-geostrophic-double-gyre-ensemble](https://earthcube2021.github.io/ec21_book/notebooks/ec21_uchida_et_al/notebooks/TU.05_Diagnosing-the-Eliassen-Palm-flux-from-a-quasi-geostrophic-double-gyre-ensemble.html)
 987 [.html](https://earthcube2021.github.io/ec21_book/notebooks/ec21_uchida_et_al/notebooks/TU.05_Diagnosing-the-Eliassen-Palm-flux-from-a-quasi-geostrophic-double-gyre-ensemble.html) doi: 10.5281/zenodo.5496375
- 988 Uchida, T., Deremble, B., & Penduff, T. (2021). The seasonal variability of the
 989 ocean energy cycle from a quasi-geostrophic double gyre ensemble. *Fluids*,
 990 6(6), 206. doi: 10.3390/fluids6060206

- 991 Uchida, T., Deremble, B., & Popinet, S. (2022). Deterministic model of the eddy dy-
 992 namics for a midlatitude ocean model. *Journal of Physical Oceanography*. doi:
 993 10.1175/JPO-D-21-0217.1
- 994 Uchida, T., Jamet, Q., Poje, A. C., & Dewar, W. K. (2021). An ensemble-based
 995 eddy and spectral analysis, with application to the Gulf Stream. *Jour-
 996 nal of Advances in Modeling Earth Systems*, 13, e2021MS002692. doi:
 997 10.1029/2021MS002692
- 998 Vallis, G. K. (2017). *Atmospheric and oceanic fluid dynamics* (2nd ed.). Cambridge
 999 University Press.
- 1000 Waterman, S., & Lilly, J. M. (2015). Geometric decomposition of eddy feedbacks in
 1001 barotropic systems. *Journal of Physical Oceanography*, 45(4), 1009–1024. doi:
 1002 10.1175/JPO-D-14-0177.1
- 1003 Xu, Y., & Fu, L.-L. (2011). Global variability of the wavenumber spectrum of
 1004 oceanic mesoscale turbulence. *Journal of Physical Oceanography*, 41(4), 802–
 1005 809. doi: <https://doi.org/10.1175/2010JPO4558.1>
- 1006 Xu, Y., & Fu, L.-L. (2012). The effects of altimeter instrument noise on the esti-
 1007 mation of the wavenumber spectrum of sea surface height. *Journal of Physical
 1008 Oceanography*, 42(12), 2229–2233. doi: 10.1175/JPO-D-12-0106.1
- 1009 Yang, P., Jing, Z., Sun, B., Wu, L., Qiu, B., Chang, P., & Ramachandran, S. (2021).
 1010 On the upper-ocean vertical eddy heat transport in the kuroshio extension.
 1011 Part I: Variability and dynamics. *Journal of Physical Oceanography*, 51(1),
 1012 229–246. doi: 10.1175/JPO-D-20-0068.1
- 1013 Young, W. R. (2010). Dynamic enthalpy, conservative temperature, and the seawater
 1014 Boussinesq approximation. *Journal of Physical Oceanography*, 40(2), 394–
 1015 400. doi: 10.1175/2009JPO4294.1
- 1016 Young, W. R. (2012). An exact thickness-weighted average formulation of the
 1017 Boussinesq equations. *Journal of Physical Oceanography*, 42(5), 692–707. doi:
 1018 10.1175/JPO-D-11-0102.1
- 1019 Zanna, L., & Bolton, T. (2020). Data-driven equation discovery of ocean
 1020 mesoscale closures. *Geophysical Research Letters*, e2020GL088376. doi:
 1021 10.1029/2020GL088376
- 1022 Zanna, L., Mana, P. P., Anstey, J., David, T., & Bolton, T. (2017). Scale-aware
 1023 deterministic and stochastic parametrizations of eddy-mean flow interaction.

1024 *Ocean Modelling*, 111, 66–80. doi: 10.1016/j.ocemod.2017.01.004

1025 Zhao, K., & Marshall, D. P. (2020). Ocean eddy energy budget and parameter-
1026 ization in the North Atlantic. In *Ocean sciences meeting*. Retrieved from

1027 <https://agu.confex.com/agu/osm20/meetingapp.cgi/Paper/646129>